ETH
Eidgenössische Technische Hochschule Zürich
Swiss Federal Institute of Technology Zurich

PAUL SCHERRER INSTITUT
PSI

Central Region Design of a Compact High Intensity Cyclotron

Master Thesis

in High Energy Physics

Department of Physics

ETH Zurich

written by

Jakob Jonnerby

supervised by

Dr. A. Adelmann (ETH)

scientific advisers

Dr. C. Baumgarten (PSI)
Dr. D. Winklehner (MIT)

September 28, 2016

Abstract

Several experiments have detected anomalies in the neutrino oscillation spectrum around 1 eV^2, indicating the existance of sterile neutrinos. The Isotope Decay at Rest (IsoDAR) project proposes to detect and determine the number of sterile neutrinos through the production of ^{8}Li, which decays at rest to give a low energy neutrino beam that is to be detected in a scintillating detector located some 10 meters from the ^{8}Li production target. ^{8}Li are produced by impinging a high-intensity proton beam into a Beryllium target surrounded by a sleeve of ^{7}Li. In this thesis, the injection and central region design of a compact high-intensity cyclotron to accelerate a H_2^+ beam up to 60 MeV/amu is considered. Beam dynamics simulations have been performed for a beam starting at 193.7 keV/amu which show that generation of a matched distribution within the first ten turns can be facilitated by collimation of the beam and optimizing the phase offset of the accelerating cavities.

Contents

List of Figures

1 Introduction and background

Neutrinos are some of the lightest and most elusive elementary particles in the standard model of particle physics. They have been studied ever since Wolfgang Pauli, professor in physics at the ETH Zurich, proposed their existence in 1930 as a way to explain the missing energy that had been observed in beta decay processes. Their low mass and the fact they are electrically neutral makes them very difficult to detect. It has been shown that there exist three flavours of neutrinos: electron, muon, and tauon neutrinos, named so depending on whether they interact with electron, muons, or tauons via the weak force. The solar neutrino problem, a discrepancy between the number of electron neutrinos that were produced in the sun and that reached the earth, gave rise to the theory of neutrino mixing between the neutrino mass states and the flavour states. In this theory, neutrinos that are produced in one neutrino flavour state can change into another flavour state as they travel through space. Many questions remain to be answered in neutrino physics, such as the exact mass of the neutrinos, the existence of sterile neutrinos that do not interact via the weak force, and whether they conserve the charge-parity symmetry that tells us if antimatter and matter behaves identically. This could potentially explain the observed matter-antimatter asymmetry in the universe, as equal amounts of matter and antimatter should have been produced in the Big Bang [7].

1.1 Neutrino oscillations, sterile neutrinos and CP-violation

The mixing between the neutrino flavour states α and mass states k is written using the neutrino mixing matrix:

$$\vec{V}_\alpha = \begin{pmatrix} c_{12}c_{13} & c_{12}c_{13} & c_{12}c_{13} \\ -s_{12}c_{23} - c_{12}s_{23}s_{13}e^{i\delta_{CP}} & c_{12}c_{13} - s_{12}s_{23}s_{13}e^{i\delta_{CP}} & s_{23}c_{13} \\ c_{12}c_{13} - c_{12}c_{23}s_{13}e^{i\delta_{CP}} & -c_{12}s_{23} - s_{12}c_{23}s_{13}e^{i\delta_{CP}} & c_{23}c_{13} \end{pmatrix} \vec{V}_k, \tag{1.1}$$

with $\alpha = e, \mu, \tau$, $k = 1, 2, 3$, $c_{ij} = \cos(\theta_{ij})$, $s_{ij} = \sin(\theta_{ij})$, and θ_{ij} the neutrino mixing angles. The CP-violating phase δ_{CP} is still unknown, and a nonzero value would indicate a difference between neutrinos and antineutrinos in terms of oscillation probability. The probability of a neutrino being produced in a flavour state α and detected in a flavor state β is written as:

$$P_{\nu_\alpha \to \nu_\beta}(L) = \sum_{k,j} U^*_{\alpha k} U_{\beta k} U^*_{\alpha j} U^*_{\beta j} \exp\left(-i \frac{\Delta m^2_{kj} L}{2E}\right), \tag{1.2}$$

where the U_{mn} refers to the matrix elements of (1.1) and $\Delta m^2_{kj} = m^2_k - m^2_j$ is the squared mass difference between the neutrino mass states k and j. L and E is the travel length and energy, respectively [7].

The Liquid Scintillator Neutrino Detector (LSND) was a neutrino oscillation experiment aimed at detecting neutrino flavor oscillations from muon antineutrinos to electron antineutrinos: $\bar{\nu}_\mu \to \bar{\nu}_e$. A beam of $\bar{\nu}_\mu$ was obtained by producing μ^+ that decayed at rest to $\bar{\nu}_\mu$. The neutrino beam then travelled a distance of 30 meters to a detector where the number of electron antineutrinos were counted.

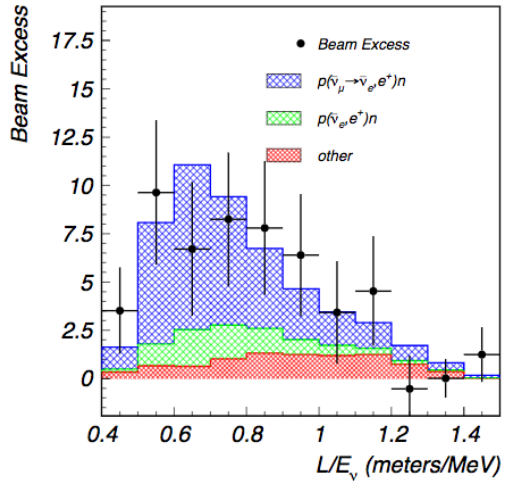

(a) LSND

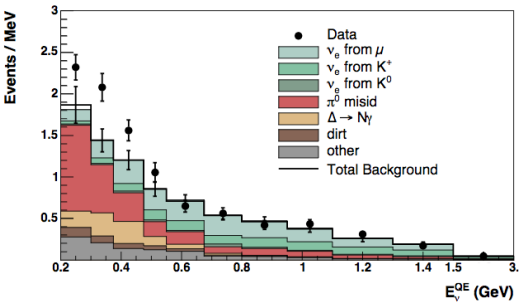

(b) MiniBooNE

Figure 1.1: The LSND and MiniBooNE neutrino beam excesses at lower energies, with the black points representing the obtained results. The green and red areas in the LSND plot represents the expected background and signal due to neutrino oscillations, and the blue area the expected results in the presence of sterile neutrinos. The colored areas in the MiniBooNE plot shows the expected background and neutrino oscillation signal without sterile neutrinos [1].

While the experiment was successful in detecting the neutrino oscillation phenomena, it observed an excess of $\bar{\nu}_e$ at lower energies that could not be explained within the framework of 3 neutrino flavors and neutrino oscillations. The Mini Booster Neutrino Experiment (MiniBooNE) at Fermilab, was constructed to test the conclusions of the LSND experiment by running at a higher energy, but with the same energy-to-distance ratio as LSND [1]. It also found a similar excess of $\bar{\nu}_e$. The results of both experiments are shown in figure 1.1. One possible explanation to the LSND and MiniBooNE results is that there exists a number of unflavoured neutrino states, called *sterile neutrinos*. These neutrinos can not be produced through the weak force, but only through neutrino oscillation. They would modify the oscillation probability by adding extra terms to the neutrino mixing matrix.

1.2 The DAEδALUS and IsoDAR projects

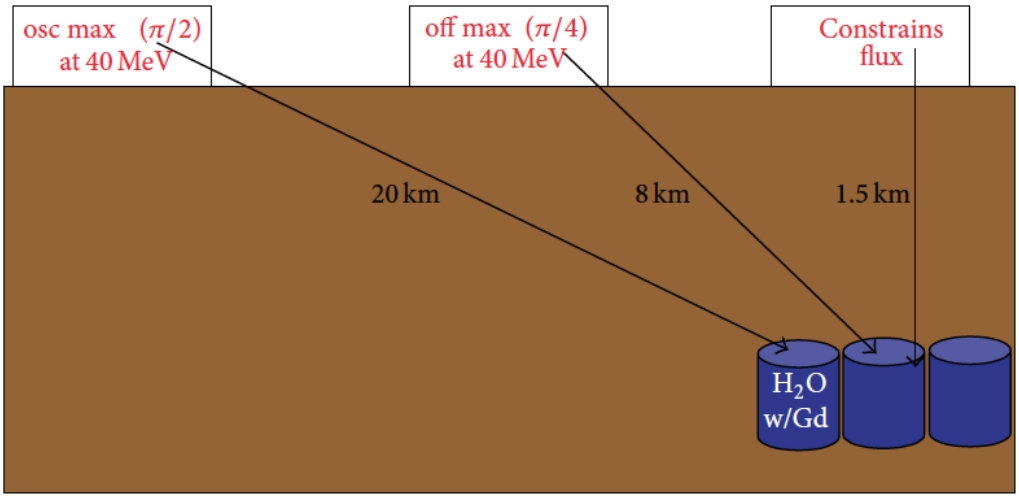

Figure 1.2: Overview of the three cyclotron sites and the common water Cherenkov detector to measure the oscillation probability as a function of distance from the three sites [2].

The Decay at Rest Experiment for δ_{CP} studies at the Laboratory for Underground Science (DAEδALUS) is an experiment to detect a CP-violating phase δ in the neutrino mixing matrix. It will use an injector cyclotron and a superconducting cyclotron to accelerate a beam up to 800 MeV/amu (atomic mass unit). By using three identical injector cyclotrons and superconducting cyclotrons located at three different sites with different distances to a water Cherenkov detector in order to normalize the beam flux, the δ_{CP}-phase can be determined. A beam of ν_μ will be produced through the decay at rest of pions and muons, and the oscillation probability to ν_e will be determined as a function of L [8]. Figure 1.2 shows a sketch of the DAEδALUS project with three cyclotron sites located at different distances from the detector. The layout of the accelerator system with a compact injector cyclotron, a superconducting ring cyclotron and a target is shown in figure 1.3.

The Isotope Decay-at-Rest (IsoDAR) experiment will be run as an intermediate project during the development phase of DAEδALUS. It would use the injector cyclotron, a target, and a scintillating detector to measure the existence and number of sterile neutrinos by measuring the disappearance probability of electron antineutrinos as a function of distance. It has been shown [3] that there is a significant difference in the shape of the oscillation probability between the one and two sterile neutrino models, see figure 1.4.

In the IsoDAR experiment, ^{8}Li isotopes will be produced at rest by bombarding a Beryllium target with 60 MeV protons. The required proton beam will be produced as H_2^+ ions in an ion source, then pre-accelerated and bunched in a radio-frequency quadrupole (RFQ) before they are injected through an electrostatic spiral inflector to a $D \approx 5$ m diameter compact cyclotron. The H_2^+ ions will then be accelerated from 35 keV/amu up to 60 MeV/amu, extracted and directed towards the beryllium target. By using H_2^+ ions the intensity of the beam can be doubled while keeping the total charge constant due to the added electron. This is important because it reduces the collective defocusing effect of the beam due to the identical charges of the particles. The

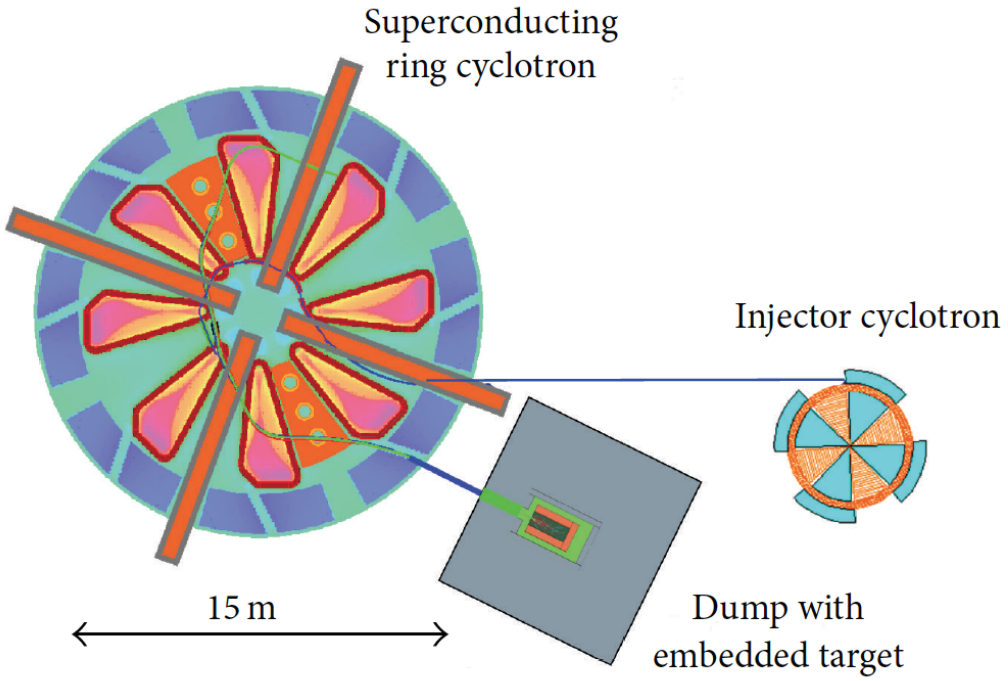

Figure 1.3: Layout of one of the DAEδALUS accelerator systems [2].

proton interaction with the beryllium produces large amounts of neutrons that interact with a surrounding layer of ^{7}Li to produce ^{8}Li by neutron capture. The ^{8}Li then quickly decays through beta decay to yield an electron neutrino beam with an average energy of 6.4 MeV and a peak energy of 9 MeV [3].

The neutrino beam will travel a short distance ($L \approx 10$ m) to a scintillating detector where the electron antineutrinos will be identified through inverse beta decay in the detector:

$$\bar{\nu}_e + p \rightarrow e^+ + n.$$

IsoDAR will use a scintillating detector with a diameter in the order of tens of meters. With a high vertex resolution capability, the number of electron antineutrinos could be tracked within the detector itself as the oscillation wavelength would be smaller than the detector, assuming a squared mass difference of 1 eV^2 [3]. This is the energy range that corresponds to the anomalous results obtained by LSND and MiniBooNE [1]. The oscillation probability as a function of distance is shown in figure 1.4 in the case of one and two sterile neutrinos. The IsoDAR cyclotron was previously simulated in [4], but excluding the central region by starting at a higher energy, 534 MeV/amu. In this thesis, the starting energy will be brought down to a third of that, 193.7 keV/amu, one turn short of the injection energy at 35 keV/amu. The results of the previous simulations are shown in figure 1.5(a) for the turn-to-turn separation and in figure 1.5(b) for the RMS beam sizes of the beam. Figure 1.6(a) shows a histogram of the particle distribution in the radial direction at the final turn in the cyclotron. The overlap of the beams at the two final turns is shown in figure 1.6(b).

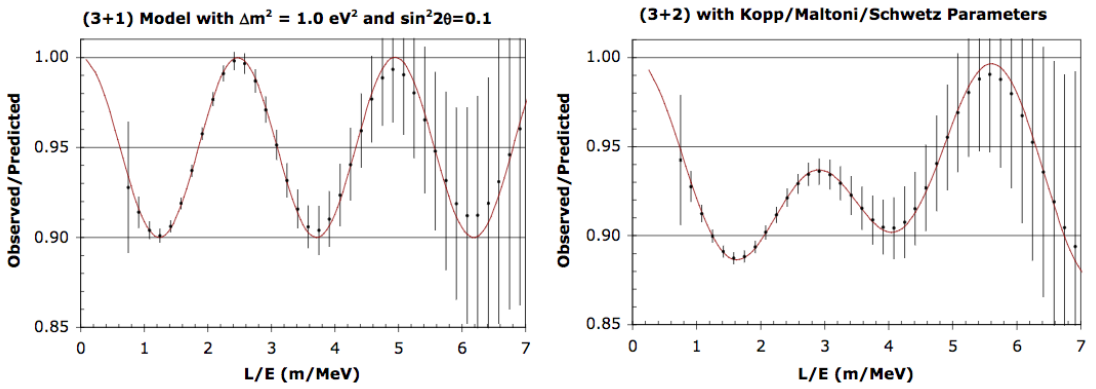

Figure 1.4: Oscillation pattern of $\bar{\nu}_\mu \to \bar{\nu}_\mu$ in the presence of one and two sterile neutrinos [3].

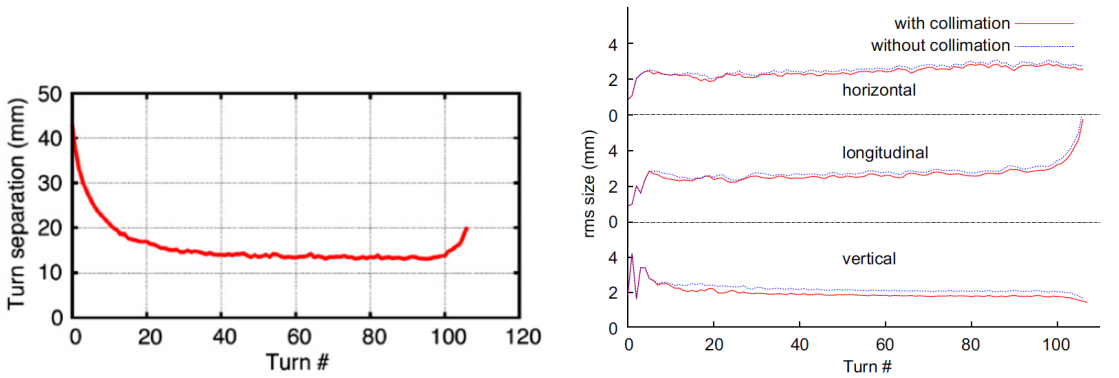

(a) Turn to to turn separation

(b) RMS beam size in the radial, longitudinal, and vertical directions

Figure 1.5: Plots of the turn-to-turn separation and RMS beam sizes presented in the paper by Yang [4], starting at an energy of 534 keV/amu.

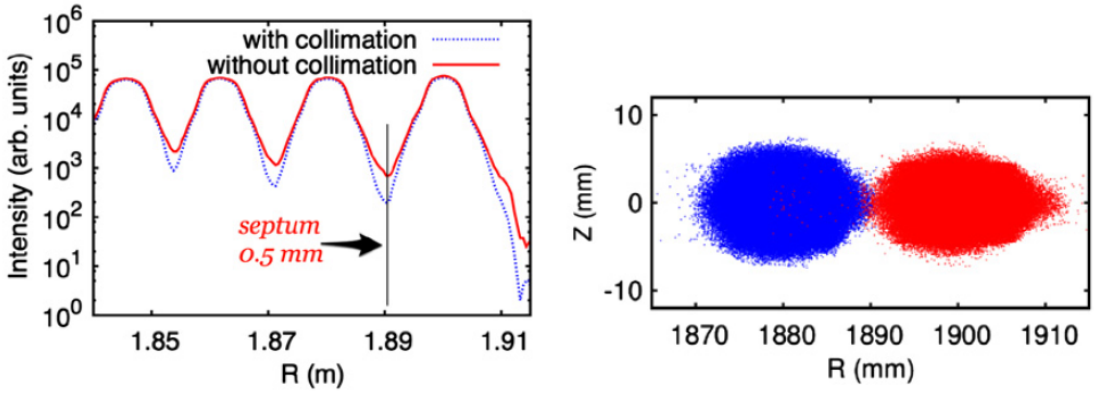

(a) Histogram of the number of particles as a function of radius

(b) Overlap of the final and next to final turn in the radial-vertical plane

Figure 1.6: Plots of the turn separation and beam overlap at the final turn of the cyclotron from the simulations by [4].

2 Theory

In this chapter a number of important theoretical aspects of a cyclotron will be introduced. First we will give a description of what the beam experiences as it goes through the accelerator, starting with the injection through an electrostatic spiral inflector. In order to find an initial position for the beam in the first turn of the cyclotron an iterative solution proposed by M.M. Gordon [9] will be described. As the H_2^+ beam travels through the cyclotron it experiences an energy gain by radio-frequency cavites that accelerate the beam up to a final energy of 60 MeV/amu. The defocusing of the beam through space charge and how it can be focused radially, vertically, and longitudinally, using the magnet structure of the cyclotron, will also be covered. In the final sections of this chapter the concepts of tunes and resonances will be studied, and how it could potentially be used to increase the final turn separation in order to safely extract the beam.

2.1 Coordinate system

In order to simplify calculations we introduce a coordinate system that is natural to particles on curvilinear trajectories through various beam elements. In these particle accelerator coordinates, known as the Frenet-Serret coordinate system, we define the trajectory of the design particle as $r_0(s)$, with s being the longitudinal coordinate along the accelerator, and any particle with a deviation of $\delta r(y)$ from this has the coordinates:

$$\vec{r}(s) = \vec{r}_0(s) + \delta\vec{r}(s).$$

The unit vectors $\vec{u}_x(s)$ and $\vec{u}_z(s)$ point in the radial and vertical directions from the design particle trajectory. The trajectory can then be written [10]

$$\vec{r}(s) = r_0(s) + x(s)\vec{u}_x(s) + z(s)\vec{u}_z(s).$$

2.2 Injection using a spiral inflector

In the IsoDAR accelerator, the H_2^+ source is located outside outside the cyclotron and the beam needs to be injected into the central region of the cyclotron. Since the beam energy is relatively low at injection, $E = 70$ keV for the H_2^+ ions, an axial injection scheme using an electrostatic spiral inflector was chosen. A spiral inflector consists of two curved electric plates with opposing voltages applied to each electrode, forming a capacitor. If the voltage applied across the electrodes matches the kinetic energy of the particle beam, the particles would travel through the centre of the gap, following the equipotential surface.

Since the central region of the cyclotron is not magnetic field-free but can be assumed to have a constant, nearly uniform component in the vertical direction, the particle is bent towards the horizontal plane it experiences a transversal force from the interaction with the magnetic field through the Lorentz force:

$$F_B = \vec{v} \times \vec{B} = v_y B_z \hat{x} - v_x B_z \hat{y}.$$

The particle is simultaneosly being bent towards the horizontal plane by the electric field and around the vertical axis by the magnetic field. The two bending radii, for the electric and magnetic fields, are [11]

$$A = \frac{mv_0^2}{qE_u}$$
$$\rho = \frac{mv_0}{qB},$$

The electrodes of the spiral inflector are therefore also to be bent to follow the trajectory of the particle for it to stay on the equipotential surface. The IsoDAR spiral inflector is shown in figure 2.1.

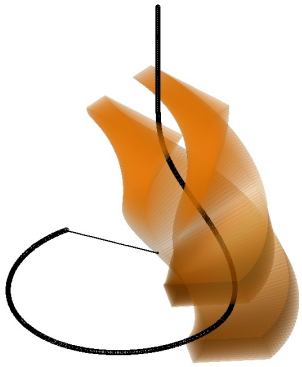

Figure 2.1: The IsoDAR spiral inflector and particle orbit [5]

2.3 Initial conditions

The radius and momentum of a single particle that for a given energy gives a closed orbit in a cyclotron can be found algorithmically by using the method described by [9]. A closed orbit is an orbit that repeats after one turn:

$$r(\theta + 2\pi) = r(\theta)$$
$$p_r(\theta + 2\pi) = p_r(\theta),$$

where r is the radius of the orbit and p_r the momentum in the radial direction. They evolve according to the following equations:

$$\frac{\mathrm{d}r}{\mathrm{d}\theta} = \frac{\mathrm{d}t}{\mathrm{d}\theta}\frac{\mathrm{d}r}{\mathrm{d}t} = \frac{rp_r}{p_\theta} \tag{2.1}$$
$$\frac{\mathrm{d}p_r}{\mathrm{d}\theta} = p_\theta = q'rB(r,\theta), \tag{2.2}$$

where p_θ is the tangential momentum and B the magnetic field. q' is defined as:

$$q' = \frac{q}{m\omega_0},$$

where ω_0 is the revolution frequency. To find the orbit $(r(\theta), p_r(\theta))$, an initial radius and momentum can be guessed as:

$$\begin{aligned} r_i &= \frac{p}{q' B_0(r)} \\ p_r &= 0, \end{aligned}$$

with B_0 the magnetic field averaged over a turn and p being the total momentum:

$$p = \gamma\beta\frac{c}{\omega_0}.$$

It will be assumed that the error in the radius and momentum will be linear after integrating the differential equations (2.2) over one full turn. We can calculate the linear error by introducing another set of differential equations, for the small deviations in r and p_r:

$$\begin{aligned} r &\to r + x \\ p_r &\to p_r + p_x. \end{aligned}$$

The corresponding differential equations for the deviations are:

$$\begin{aligned} \frac{\mathrm{d}x}{\mathrm{d}\theta} &= \frac{p_r}{p_\theta}x + \frac{rp^2}{p_\theta^3}p_x \\ \frac{\mathrm{d}p_x}{\mathrm{d}\theta} &= -\frac{p_r}{p_\theta} - q'\left[B + r\frac{\partial B}{\partial r}\right]x. \end{aligned}$$

Solving for two different starting conditions allows us to write down the transfer matrix X:

$$X(\theta, \theta_i) = \begin{pmatrix} x_1(\theta) & x_2(\theta) \\ p_{x_1}(\theta) & p_{x_2}(\theta) \end{pmatrix} \equiv \begin{pmatrix} x_1 & x_2 \\ p_{x_1} & p_{x_2} \end{pmatrix}_\theta.$$

After integrating over one turn, the radius and orbital momentum errors are:

$$\epsilon_1 = r(\theta_f) - r_i \tag{2.3}$$
$$\epsilon_2 = p_r(\theta_f) - p_{r_i}. \tag{2.4}$$

Through the assumption of having only linear error terms, this translates into an error on the initial guess in the following way:

$$\begin{pmatrix} r_c \\ p_{rc} \end{pmatrix}_\theta = \begin{pmatrix} r \\ p_r \end{pmatrix}_\theta + X(\theta, \theta_i)\begin{pmatrix} \delta r \\ \delta p_r \end{pmatrix}, \tag{2.5}$$

where the subscript c refer to the initial coordinates of the closed orbit. By using the definition of the errors in (2.4) and taking the difference between the equation (2.5) applied at $\theta = \theta_i$ and $\theta = \theta_f$ we get the following equation:

$$0 = \begin{pmatrix} \epsilon_1 \\ \epsilon_2 \end{pmatrix} + [X(\theta_f, \theta_i) - 1] \begin{pmatrix} \delta r \\ \delta p_r \end{pmatrix}.$$

From this we can calculate the correction terms as:

$$\delta r_i = \frac{(X_{22} - 1)\epsilon_1 - X_{12}\epsilon_2}{X_{11} + X_{22} - 2}$$
$$\delta p_{r_i} = \frac{(X_{11} - 1)\epsilon_2 - X_{21}\epsilon_1}{X_{11} + X_{22} - 2}.$$

Using these values, a new guess for the initial coordinates is then given as

$$r_i \to r_i + \delta p_{ri}$$
$$p_{r_i} \to p_{r_i} + \delta p_{r_i}.$$

If the first guess was close enough to the correct initial position, this method will converge to that initial position. In a similar way, the correct starting position in the vertical dimension can be calculated.

2.4 Acceleration

In the cyclotron, the H^+ ions are accelerated through RF-cavities located in the valley regions of the machine, between the magnets. The RF cavities have a frequency of 49.2 MHz, which is exactly 6 times higher than the cyclotron frequency, i.e. is running at harmonic 6. This means that six bunches can be accelerated simultaneously within one turn in the cyclotron. There is a peak voltage of 250 kV of the fields inside the cavities. The cavity gaps are located at 31, 59, 121, 149, 211, 239, 301, and 329 degrees azimuthally, forming four sets of cavities with one Dee each.

The energy gain the particle experiences is calculated analytically through the peak voltage at a given radius (as shown in figure 2.2) times the phase factor and times the time transit factor. The phase factor is given by $\cos(\phi_0 - \omega t)$ where ϕ_0 is an offset phase and ωt is the acquired phase by the particle as it circulates in the machine. The time transit factor is calculated from the gapwidth of the cavity and accounts for the fact that the RF phase varies while the particle is inside the cavity. This factor can be calculated by writing the time t as a function of distance z:

$$t(z) = \int_0^z \frac{dz}{v(z)},$$

where $v(z)$ is the velocity of the particle. We assume that for a relativistic particle the velocity does not change through the accelerating gap, and thus:

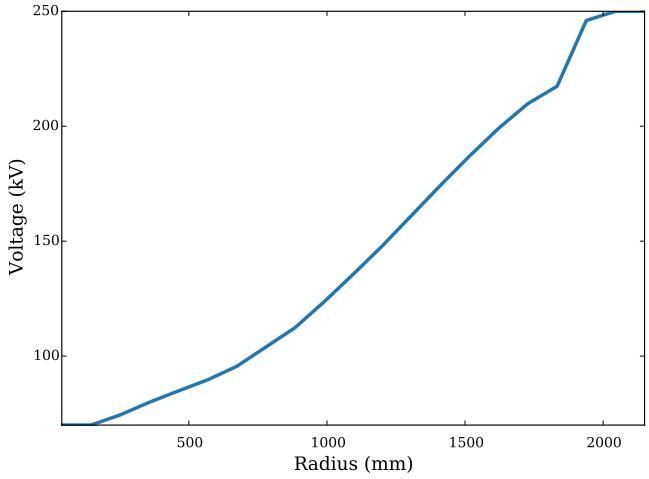

Figure 2.2: Voltage profile in the radial direction of the RF cavities in the IsoDAR cyclotron [6].

$$t(z) \approx \frac{z}{\beta c}.$$

Then we can rewrite the ωt-term in the phase factor:

$$\omega t = 2\pi f t \approx \frac{2\pi c}{\lambda}\frac{z}{\beta c} = \frac{2\pi z}{\beta\lambda},$$

with f the frequency and λ the wavelength of the accelerating wave. We can write the energy gain from a single gap crossing as:

$$\begin{aligned}\Delta E &= qV \int_{-L/2}^{L/2} \cos(\phi_0 - \omega t_0 - \omega t(z))\,\mathrm{d}z \\ &\approx qV \int_{-L/2}^{L/2} \cos(\phi_0 - \omega t_0)\cos\left(\frac{2\pi z}{\beta\lambda}\right) - \sin(\phi_0 - \omega t)\sin\left(\frac{2\pi z}{\beta\lambda}\right)\mathrm{d}z,\end{aligned}$$

where the center of the gap is located at $z = 0$ and the gap half-length is L. We have subtracted t_0, the time when the particle is in the centre of the cavity, from the time $t(z)$. The second term in the integral is odd and the integral is therefore is equal to zero. We integrate the first term as:

$$\begin{aligned}\Delta E &= qV\cos(\phi_0 - \omega t_0)\left[\sin\left(\frac{2\pi z}{\beta\lambda}\right)\frac{\beta\lambda}{2\pi}\right]_{L/2}^{-L/2} \\ &= qV\cos(\phi_0 - \omega t_0) 2\sin\left(\frac{L\pi}{\beta\lambda}\right)\frac{\beta\lambda}{2\pi},\end{aligned}$$

where we can now identify the time transit factor:

$$T = \sin\left(\frac{L\pi}{\beta\lambda}\right)\frac{\beta\lambda}{\pi},$$

and the final expression for the energy gain through a single cavity gap is [12]

$$\Delta E = qV\cos(\phi_0 - \omega t_0)T.$$

2.5 Space charge

Since the particle beam consist of ions with the identical charge the beam is defocused due to space charge. The defocusing depends on the total beam current, the beam energy, and the size of the bunch. For a uniform charge distribution, the charge density is

$$\rho = \frac{I}{a^2\pi\beta c},$$

where a is the radius of the beam, I the beam current, c the speed of light and $\beta = v/c$. The electric field can then be calculated by integrating

$$\begin{aligned}
\vec{\nabla}\cdot\vec{E} &= \rho \\
\int \vec{\nabla}\cdot\vec{E}\mathrm{d}V &= \int \rho \mathrm{d}V \\
\int \vec{E}\cdot\mathrm{d}\vec{S} &= \int \rho \mathrm{d}V,
\end{aligned}$$

where Gauss' theorem was used to pass to the last line. For an infinite cylinder with radius a this yields the electric field:

$$\begin{aligned}
E_r &= \frac{I}{2\pi\epsilon_0 a^2 v}r \qquad r \leq a \\
E_r &= \frac{I}{2\pi\epsilon_0 v r} \qquad r > a,
\end{aligned}$$

where v is the velocity of the beam, r the radius at which we are measuring the electric field, and ϵ_0 the free space permittivity. We get the resulting magnetic field from Ampre's law:

$$\begin{aligned}
\int \vec{B}\cdot\mathrm{d}\vec{l} &= \mu_0 \int \vec{J}\cdot\mathrm{d}\vec{S} \\
\Rightarrow B_\theta &= \mu_0\frac{Ir}{2\pi a^2} \qquad r < a \\
B_\theta &= \mu_0\frac{I}{2\pi r} \qquad r > a,
\end{aligned}$$

where J is the current density. The Lorentz force acting on a single particle is, due to the symmetry of the geometry considered, given by:

Table 2.1: IsoDAR and Injector II beam energy and power at injection.

Parameter (at injection)	IsoDAR [3]	Injector II (PSI) [14]
E_{kin}	35 keV/amu	870 keV
β	$8.64e-3$	0.0136
γ	1.000037	1.0000927
I	5 mA	3 mA
mc^2	1876 MeV	938 MeV
K	9.9	5.1

$$\begin{aligned}
\frac{\mathrm{d}p}{\mathrm{d}t} &\approx \gamma m\ddot{r} = F_L \\
\gamma m\ddot{r} &= q(E_r - q\dot{z}B_\theta) \\
\gamma m\ddot{r} &= \frac{qIr}{2\pi\epsilon_0 a^2 \beta c}(1-\beta^2),
\end{aligned}$$

where q is the charge of the ion, m its mass, and γ the lorentz factor. This gives the following differential equation in the radial direction for a single particle due to the space charge of the bunch:

$$\ddot{r} = \frac{qI}{2\pi\epsilon_0 a^2 mc^3\beta^3\gamma^3} r,$$

where we have used the fact that $1-\beta^2 = \gamma^{-2}$. We can also put this equation in the simple form:

$$\ddot{r} = \frac{K}{a^2} r,$$

where we have introduced the generalized perveance K, which only depends on the total charge of the beam, the beam energy, and the type of ion [13]:

$$K = \frac{qI}{2\pi\epsilon_0 mc^3\beta^3\gamma^3}.$$

For the IsoDAR cyclotron, the relevant parameters for the perveance are shown in table 2.1. This gives a generalized perveance of $K \approx 10$, which is a factor 2 larger than what have been achieved in similar projects such as Injector II at PSI.

2.6 Transverse focusing

In the simple case of a traditional cyclotron the transverse, meaning radial and vertical, focusing is achieved by a radially varying magnetic field. Consider a particle in a cyclotron with global coordinates (ρ, θ, z) and $x \ll \rho$ a small deviation in the radial direction. The particles total radius is then [15]

$$r = \rho + x = \rho\left(1 + \frac{x}{\rho}\right).$$

The magnetic field in z direction is non-uniform, and it can be expanded in the direction of x by:

$$B_z = B_{0,z} + \frac{\partial B_0}{\partial x}x = B_{0,z}\left(1 + \frac{\rho}{B_0}\frac{\partial B_z}{\partial x}\frac{x}{\rho}\right), \tag{2.6}$$

where $B_{0,z}$ is a constant magnetic field. We can now define the field index:

$$n = -\frac{\rho}{B_{0,z}}\frac{\partial B_z}{\partial x}, \tag{2.7}$$

which we use to rewrite (2.6):

$$B_z = B_{0,z}\left(1 - n\frac{x}{\rho}\right).$$

Next we calculate the forces acting on the particle in the radial direction. In this simple example, we are only considering the outward centrifugal force and the restoring force from the magnetic field in the case of so-called weak focusing. The centrifugal force can be written in the nonrelativistic case:

$$F_C = \frac{mv_\theta^2}{r} = \frac{mv_\theta^2}{\rho}\frac{1}{(1+\frac{x}{\rho})} \approx \frac{mv_\theta^2}{\rho}\left(1 - \frac{x}{\rho}\right),$$

where v_θ is the tangential velocity of the particle. The Lorentz force caused by the charged particle motion in the cyclotron magnetic field is, using the expansion (2.6):

$$F_L = -qv_\theta B_z = -qv_\theta B_{0,z}\left(1 - n\frac{x}{\rho}\right).$$

Comparing the two forces yields:

$$F_X = F_C - F_L = \frac{mv_\theta^2}{\rho}\left(1 - \frac{x}{\rho}\right) - qv_\theta B_{0,z}\left(1 - n\frac{x}{\rho}\right).$$

The first to terms correspond to the unperturbed motion and therefore cancel out. The remaining two terms yield the following expression:

$$F_X = -\frac{mv_\theta^2}{\rho}\frac{x}{\rho}(1-n).$$

The particle motion from this force is $F_X = m\ddot{x}$, so that we get

$$\ddot{x} + \frac{v_\theta^2}{\rho}\frac{x}{\rho}(1-n) = 0. \tag{2.8}$$

This is the equation for the harmonic oscillator, where the oscillation frequency is given by

$$\omega = \sqrt{1-n}\frac{v_\theta}{\rho} = \sqrt{1-n}\omega_0,$$

with $\omega_0 = v_\theta/\rho$. This means that in order for the particle motion to be stable in the horizontal plane, the oscillation frequency must be real, and therefore $n < 1$. This is true in a uniform field, for which $n = 0$. In the vertical plane, there is no centrifugal force so the restoring force is:

$$F_Z = qv_\theta B_x = m\ddot{z}.$$

If the vertical magnetic field varies in the radial direction there is also magnetic field in the x-direction because the curl of the field is zero and so we have that:

$$\vec{\nabla} \times \vec{B} = 0 \Rightarrow \frac{\partial B_x}{\partial z} = \frac{\partial B_z}{\partial x}.$$

This gives a magnetic field in the x-direction along z is:

$$B_x \approx \frac{\partial B_x}{\partial z}z = -n\frac{B_0}{\rho}z.$$

This gives another harmonic equation of motion:

$$\ddot{z} + \omega_z z = 0, \tag{2.9}$$

with frequency:

$$\omega_z = \sqrt{n}\omega_0.$$

The condition that the motion is bounded this time is that $n > 0$, so for a uniform magnetic field with $n = 0$ there is no vertical focusing. In a weak focusing cyclotron we finally see that $0 < n < 1$, in order to have focusing in both planes. However, in the relativistic case these conditions can not be simultaneously satisfied if isochronicity is to be conserved in the cyclotron. The reason for that is that the revolution frequency changes with energy:

$$\omega_{rev} = \frac{qB(r)}{\gamma(r)m},$$

where $\gamma = (1-\beta)^{-1}$ is the Lorentz factor, m the mass, and $\beta = v/c$ the fractional speed of light. The dependency on r indicates that the radius of the motion depends on the energy. As γ increases through acceleration, the magnetic field B also has to increase radially. This would require a negative field index n, and so is not compatible with the condition for vertical stability.

This limits the energy that can be reached with a cyclotron using the principle of weak focusing to nonrelativistic energies only.

A solution to this is to use a segmented magnet structure, known as azimuthally varying field (AVF). In this cyclotron model, low-field regions (valleys) are followed by regions of high-field regions (hills). The particles no longer follow a circular trajectory but are more strongly bent in the hills and less bent in the valleys. Between the valleys and hills an azimuthal magnetic field appears, and it is this field together with the radial velocity that gives vertical focusing. The magnetic field of the IsoDAR cyclotron is shown in figure 2.3 as a representation of such a field structure. For the focusing, we see that:

$$\nabla \times \vec{B} = 0 \Rightarrow \frac{1}{\rho}\frac{\partial B_z}{\partial \theta} = \frac{\partial B_\theta}{\partial z},$$

and the Lorentz force gives the restoring force in the vertical direction [15]

$$F_Z = -rB_\theta \approx -\frac{\partial B_z}{\partial \theta} z.$$

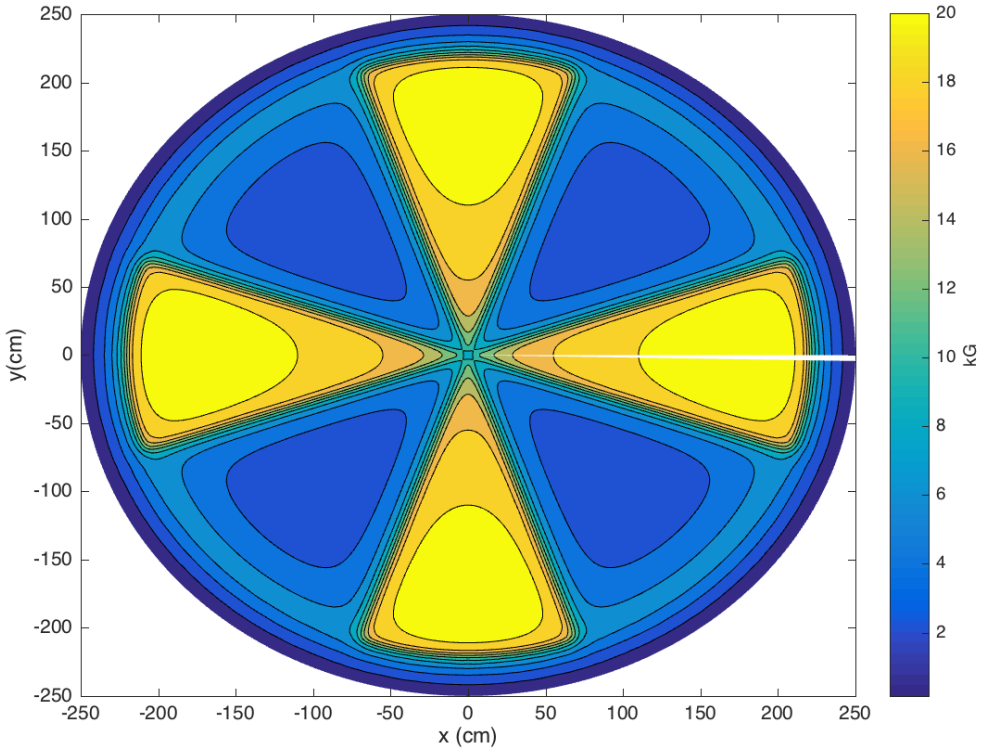

Figure 2.3: Magnetic fieldmap of the IsoDAR compact cyclotron [6]

2.7 Longitudinal focusing

In an isochronous cyclotron, there is no external longitudinal focusing since particles of all energies have the same revolution frequency. In a synchronous accelerator, such as a synchrotron, particles that arrive before or after the synchronous phase get a slightly larger or smaller energy kick that causes them to catch up with the centre of the bunch.

There is however an effect known as vortexing in isochronous cyclotrons when the space charge is important. Due to space charge, the particles in front of the bunch are pushed forward and the particles in the back backward, making them gain and lose a small amount of energy, respectively. This causes the front particles to go on a higher radius and the back particles on a lower radius. To see that this leads to focusing we start with the Hamiltonian of the beam in local coordinates and expanded to second order, including space charge and focusing [16]

$$H = \frac{x'^2}{2} + \frac{\delta^2}{2\gamma^2} + \frac{k_x - K_x}{2}x^2 - \frac{\gamma^2 K_z}{2}l^2 - hx\delta,$$

where $\gamma = (1-\beta)^{-1}$, x the deviation in the radial direction, x' the derivative with respect to s $x' = \frac{\mathrm{d}x}{\mathrm{d}s}$, l the longitudinal deviation and $\delta = \frac{p-p_0}{p_0}$ is the deviation from the design energy. h is defined as the inverse bending radius $h = \frac{1}{r}$, k_x the restoring force $k_x = h^2(1+n)$, where n is the field index as before. K_x and K_z are the space charge perveances in radial and vertical directions. The equations of motion can then be found from:

$$\begin{aligned}
\frac{\mathrm{d}x}{\mathrm{d}s} &= \frac{\partial H}{\partial x'} = x' \\
\frac{\mathrm{d}x'}{\mathrm{d}s} &= -\frac{\partial H}{\partial x} = (k_x - K_x)x \\
\frac{\mathrm{d}l}{\mathrm{d}s} &= \frac{\partial H}{\partial \delta} = \frac{\delta}{2\gamma^2} \\
\frac{\mathrm{d}\delta'}{\mathrm{d}s} &= -\frac{\partial H}{\partial l} = \gamma^2 K_x.
\end{aligned}$$

This can be written in form of a matrix:

$$\frac{\mathrm{d}}{\mathrm{d}s}\begin{pmatrix} x \\ x' \\ l \\ \delta \end{pmatrix} = \begin{pmatrix} 0 & 1 & 0 & 0 \\ -k_x + K_x & 0 & 0 & h \\ -h & 0 & 0 & \frac{1}{\gamma^2} \\ 0 & 0 & K_z\gamma^2 & 0 \end{pmatrix}\begin{pmatrix} x \\ x' \\ l \\ \delta \end{pmatrix}.$$

The eigenvalues of this matrix are:

$$\vec{\lambda} = (i\Omega, -i\Omega, i\omega, -i\omega),$$

where Ω and ω have been defined as

$$\begin{aligned}
\Omega &= \sqrt{a + \sqrt{a^2 - b}} \\
\omega &= \sqrt{a - \sqrt{a^2 - b}},
\end{aligned}$$

and a and b are:

$$a = \frac{k_x - K_x - K_z}{2}$$
$$b = K_z(K_x + h^2\gamma^2 - k_x).$$

To see how space charge can affect the stability of the beam, we can see that the solution of a linear equation of motion in matrix form as:

$$x'(s) = Fx(s),$$

the solution of which is:

$$x(s) = \exp(Fs)x(0) = M(s)x(0).$$

Here M is the so-called transfer matrix. The diagonal matrix with the eigenvectors of F can be used together with an invertible transformation matrix E to express F as

$$F = E\lambda E^{-1}.$$

Similarly, M can be written as

$$M = E\exp(\lambda s)E^{-1},$$

so that the eigenvalues of F corresponds to the phases of M. Then, in order for the motion to remain bounded, each phase must be real and therefore the following criterion has to be satisfied:

$$b > 0 \Rightarrow K_z(K_x + h^2\gamma^2 - k_x) > 0.$$

We can evaluate the term $k_x = h^2(1-n)$, where the field index, as before, is defined as:

$$n = -\frac{r}{B}\frac{\mathrm{d}B}{\mathrm{d}r}.$$

We also consider adding a small field error $\epsilon(r)$ to the magnetic field for an isochronous cyclotron:

$$B(r) = B_0\frac{1+\epsilon(r)}{1-\beta^2}.$$

The field index can then be written approximately as:

$$n \approx -r\frac{\mathrm{d}\epsilon}{\mathrm{d}r} - \gamma^2 + 1.$$

Inserted into the equation for the focusing k_x:

$$k_x = h^2 \left(r\frac{\mathrm{d}\epsilon}{\mathrm{d}r} + \gamma^2 \right) = h^2\gamma^2 + h\frac{\mathrm{d}\epsilon}{\mathrm{d}r},$$

so that the b becomes:

$$b = K_z \left(K_x - h\frac{\mathrm{d}\epsilon}{\mathrm{d}r} \right).$$

This means that the space charge in the radial direction must be $K_x > h\frac{\mathrm{d}\epsilon}{\mathrm{d}r}$ to ensure focusing in the longitudinal direction [16]. This means that the bigger the magnet imperfections are, the higher the space charge must be to ensure longitudinal focusing.

2.8 Matched distribution

To find a description suitable for describing beam distributions, we start by defining the particle state vector:

$$\vec{x} = (x, px, y, py, z, pz)^T,$$

so that we could define the sigma matrix, which consists of all second-order moments of the beam distribution:

$$\sigma = \langle \vec{x}\vec{x}^T \rangle.$$

$$\sigma = \begin{pmatrix} \langle xx \rangle & \langle xp_x \rangle & \langle xz \rangle & \langle xp_z \rangle & \langle xy \rangle & \langle xp_y \rangle \\ \langle p_x x \rangle & \langle p_x p_x \rangle & \langle p_x z \rangle & \langle p_x p_z \rangle & \langle p_x y \rangle & \langle p_x p_y \rangle \\ \langle zx \rangle & \langle zp_x \rangle & \langle zz \rangle & \langle zp_z \rangle & \langle zy \rangle & \langle zp_y \rangle \\ \langle p_z x \rangle & \langle p_z p_x \rangle & \langle p_z z \rangle & \langle p_z p_z \rangle & \langle p_z y \rangle & \langle p_z p_z \rangle \\ \langle yx \rangle & \langle yp_x \rangle & \langle yz \rangle & \langle yp_z \rangle & \langle yy \rangle & \langle yp_y \rangle \\ \langle p_y x \rangle & \langle p_y p_x \rangle & \langle p_y z \rangle & \langle p_y p_z \rangle & \langle p_y y \rangle & \langle p_y p_y \rangle \end{pmatrix}.$$

Since the cyclotron is symmetric around the midplane, the vertical motion is decoupled from the radial and longitudinal motions and all vertical-radial and vertical-longitudinal cross-terms such as $\langle xz \rangle$ and $\langle yz \rangle$ are zero. The state vector after one turn can be determined by the transfer map:

$$\vec{x}_f = M\vec{x}_i.$$

So that the sigma matrix after one turn is:

$$\sigma_f = \langle \vec{x}_f \vec{x}_f^T \rangle = \langle M\vec{x}_i \vec{x}_i^T M^T \rangle = M\sigma_i M^T,$$

if $\sigma_f = \sigma_i$, the beam distribution is identical after one turn in the cyclotron and is said to be matched. A module for finding a matched distribution for a coasting beam has been implemented in the particle accelerator simulation programme OPAL by [17].

2.9 Tunes and resonances

As the particles moves around the accelerator they undertake a number of oscillations around the design particle trajectory, known as precessional movement. The number of such oscillations is called the tune, and we can investigate this by noting that we can find particular solutions to equations (2.8) and (2.9):

$$x(t) = x_0 \cos(\nu_r \omega_0 t) \tag{2.10}$$
$$z(t) = z_0 \cos(\nu_z \omega_0 t) \tag{2.11}$$

Since ω_0 is the revolution frequency of the particle, the tune tell us the frequency of the vertical and radial oscillations as a function of the revolution frequency. For example, if we have for the radial tune $\nu_r = 2$, it means that the particle is oscillating around the design trajectory with the twice the frequency of the revolution frequency so that for every turn it completes two complete radial oscillations [15]. We can see this by considering a small n-th order perturbation on the motion [18]

$$\ddot{x} + \nu^2 \omega^2 x = p_n(\phi) x^{n-1}, \tag{2.12}$$

where p_n is a periodic n-th order perturbation, which depends on the phase $\phi = \omega_0 t$. It has the following Fourier series:

$$p_n(\phi) = \sum_m p_{nm} \mathrm{e}^{-im\phi}. \tag{2.13}$$

Furthermore, we assume that the perturbed orbit is small so that we can replace x^{n-1} with the unperturbed orbit x_0^{n-1} from (2.10). Then we also expand x_0 to its Fourier series:

$$x_0^{n-1}(\phi) = \sum_{|q| \leq n-1} W_q \mathrm{e}^{-iq\nu_0\phi}. \tag{2.14}$$

Inserting (2.13) and (2.14) into (2.12) yields:

$$\ddot{x} + \nu^2 \omega^2 x = \sum_{mq} p_{nm} W_q \mathrm{e}^{-i(m+q\nu_0)\phi}. \tag{2.15}$$

This induces a resonance whenever

$$\nu_0 = m + q\nu_0,$$

i.e. when the eigenfrequency of the unperturbed motion is equal to the frequency of the perturbation. When we have a first-order perturbation, $q = 0$ and the motion will be unstable whenever the tune is an integer: $\nu_0 = m$. For a second order perturbation, q is either $q = \pm 1$ or $q = 0$. For example, from the term $q = -1$ we get:

$$2\nu_0 = m,$$

so that we have a resonance when ν_0 is either an integer or a half-integer [18].

2.10 Turn-to-turn separation and extraction

In order to reduce overlaps of beam bunches of different turns, it is necessary to maximize the turn-to-turn radial separation of the orbit. The turn-to-turn separation has two components, from the acceleration and from precessional motion. First, we will derive the expression for the turn separation due to acceleration.

In an isochronous cyclotron, the magnetic field in z-direction increases radially in order to keep the revolution frequency constant with increasing energy. The magnetic field, orbit radius and particle momentum are related through the *magnetic rigidity*. A charged particle travelling on a circular trajectory in a constant magnetic field would experience the following force:

$$F_r = \frac{\mathrm{d}p}{\mathrm{d}t} = p\dot{\theta}$$
$$F_r = p\frac{v_\theta}{R},$$

which is equal to the Lorentz force, with $B = B_z$:

$$F_L = qv_\theta B$$
$$F_r = F_L \Rightarrow ev_\theta B = p\frac{v_\theta}{R}$$
$$\Rightarrow BR = \frac{p}{e}.$$

We write this as:

$$BR = \frac{p}{e} = \frac{mc\gamma\beta}{e} = \sqrt{1-\frac{1}{\gamma^2}}\gamma\frac{mc}{e} = \sqrt{\gamma^2-1}\frac{mc}{e}.$$

The we can calculate the logarithmic differential of the left and right hand sides by differentiating by $\mathrm{d}R\mathrm{d}B\mathrm{d}\gamma$ and dividing by $BR\gamma$. This gives:

$$\text{(LHS): } \frac{1}{BR\gamma}(R\mathrm{d}B + B\mathrm{d}R) = \frac{1}{\gamma}\left(\frac{\mathrm{d}B}{B} + \frac{\mathrm{d}R}{R}\right)$$
$$\text{(RHS): } \frac{1}{BR\gamma}\frac{\gamma\mathrm{d}\gamma}{\sqrt{\gamma^2-1}}\frac{mc}{e} = \frac{1}{\gamma}\frac{\gamma\mathrm{d}\gamma}{(\gamma^2-1)}.$$

Combining the RHS and LHS from the equation above gives us:

$$\frac{\mathrm{d}B}{B} + \frac{\mathrm{d}R}{R} = \frac{\gamma\mathrm{d}\gamma}{(\gamma^2-1)}.$$

Eliminating the B-term by using the expression for the field index in (2.7) gives:

$$\frac{\mathrm{d}B}{B} = -\frac{\mathrm{d}R}{R}n \tag{2.16}$$

$$\Rightarrow \frac{\mathrm{d}R}{R}(1-n) = \frac{\gamma \mathrm{d}\gamma}{(\gamma^2-1)} \tag{2.17}$$

$$\Rightarrow \frac{\mathrm{d}R}{R} = \frac{\gamma \mathrm{d}\gamma}{(\gamma^2-1)(1-n)} \tag{2.18}$$

$$\Rightarrow \frac{\mathrm{d}R}{\mathrm{d}\gamma} = \frac{\gamma R}{(\gamma^2-1)(1-n)}. \tag{2.19}$$

We now have an expression for the variation of the radius with respect to the Lorentz factor. The Lorentz factor in turn depends on the energy, so that if we know the energy gain per turn we could calculate the radius gain per turn. The energy gain per turn is known from the design of the machine, and we represent it by $\frac{\mathrm{d}E}{\mathrm{d}N_t} = U_t$. The Lorentz factor and its derivative with respect to the energy can be expressed as:

$$\gamma = \frac{E}{mc^2} \tag{2.20}$$

$$\frac{\mathrm{d}\gamma}{\mathrm{d}E} = \frac{1}{mc^2} \tag{2.21}$$

$$\Rightarrow \frac{\mathrm{d}\gamma}{\mathrm{d}N_t} = \frac{U_t}{mc^2}, \tag{2.22}$$

We can express the derivative of the radius with respect to the number of turns as:

$$\frac{\mathrm{d}R}{\mathrm{d}N_t} = \frac{\mathrm{d}R}{\mathrm{d}\gamma}\frac{\mathrm{d}\gamma}{\mathrm{d}N_t},$$

into which we can insert the expressions obtained in (2.19) and (2.22):

$$\frac{\mathrm{d}R}{\mathrm{d}N_t} = \frac{\gamma R}{(\gamma^2-1)(1-n)}\frac{U_t}{mc^2}. \tag{2.23}$$

The field index n is related to the radial and longitudinal tunes ν_r and ν_l. The radial tune is given by $\nu_r = \sqrt{1-n}$. This gives another way to write equation (2.23) in terms of the radial tune:

$$\frac{\mathrm{d}R}{\mathrm{d}N_t} = \frac{\gamma R}{(\gamma^2-1)\nu_r^2}\frac{U_t}{mc^2}. \tag{2.24}$$

In order to increase the radial turn-to-turn separation, it is possible to reduce the tune ν_r by decreasing the magnetic field index in the last couple of turns. This however means that isochronicity is lost [19].

So far, we only considered the turn-to-turn separation due to acceleration. In order to extract the beam we need to increase the separation for the last turn in order to insert an extracting septum between the final and the next-to-final turns. One way to achieve this is to is insert a first-order harmonic in the magnetic field so that the beam passes through the $\nu_r = 1$ resonance. This produces a second term in the turn-to-turn separation equation, namely:

Table 2.2: Values of the parameters relevant for the final turn separation

Parameter	Value	Unit
R	1879	mm
γ	1.0645	
U_t	1.79	MeV
ν_r	0.984	
mc^2	1876	MeV

$$\frac{\mathrm{d}R}{\mathrm{d}n}_{\text{precession}} = 2x_c \sin(\pi(1-\nu_r)),$$

where x_c is the amplitude increase:

$$x_c = \pi R \frac{b_1}{B_0} n_{\text{eff}},$$

with b_1 the field strength of the harmonic and n_{eff} the "effective" field index:

$$n_{\text{eff}} = \frac{1}{\sqrt{\left|\frac{\mathrm{d}\nu_r}{\mathrm{d}n}\right|}}.$$

To extract the bunch in the final turn of the cyclotron, a grounded metal sheet called a septum is inserted between the last two turns. Another metal plate, located on the outside of the final turn, has a voltage applied to it which creates a deflecting electrostatic field between the two plates. This causes the bunch to be bent out from the cyclotron [11]. In order to evaluate the turn separation in the IsoDAR cyclotron analytically, we insert the values from table 2.2 into the formula for turn separation in equation (2.24). This gives a turn separation at the final turn of 14.7 mm.

3 Simulations

The simulations of the IsoDAR cyclotron was divided into two separate parts: the central region, consisting of the spiral inflector and three of the RF cavities during the first turn, and the main cyclotron, starting from the first turn up to extraction. The reason for this was that the simulation in these two regions use different fieldmaps for the magnets and RF-cavities, as well as different field solvers. In the central region, a full 3D-model was used for the magnetic fields and the spiral inflector. In the outer region, starting from an azimuthal angle of $\Theta = -135$ the field map for the spiral inflector was removed while 1D-fieldmaps were used for the RF cavities and a 2D fieldmap was used for the cyclotron magnetic field. These fieldmaps only contained values at the midplane ($z = 0$), which OPAL then interpolated to values below and above the midplane.

In the central region a single particle was injected through the electrostatic spiral inflector and accelerated using the 1D cavity models. The 1D cavity models could not be used for simulating a particle bunch, because OPAL did not allow mixing 1D cavity models with the full 3D geometry of the central region.

In the outer region of the cyclotron simulations were performed both with a single particle and a particle bunch. The single particle simulations served two purposes; to find good initial conditions in terms of initial radius, orbital momentum, and RF phase offset, and to analyze the orbit in terms of turn-to-turn separation, tunes, and vertical oscillations. The particle bunch simulations used the initial conditions found by the single particle simulations, but also required parameters related to the distribution of particles within the bunch.

In this chapter will be described how the best values for all these parameters were determined. While this does not constitute a full parameter study of the problem, it does serve as to give some intuition into how this parameter space looks like.

3.1 OPAL

The simulations were performed using the computer program OPAL (Object Oriented Parallel Accelerator Library) on a high performance computing cluster at the Paul Scherrer Institute, Switzerland. For cyclotron simulations, OPAL can be used to track 3D particle bunches with space charge using either analytic or real field maps for the magnet structure and RF cavities [20].

3.2 Single particle simulations

In order to determine the best initial paramater values at $\theta = -135$, the particle was first injected and accelerated with an energy of 193 keV/amu and the orbit analyzed with respect to the turn-to-turn separation. If the initial conditions were correct, this would lead to a constant turn separation throughout the trajectory. With incorrect initial conditions this would lead to an orbit where the turn separation would not be at a constant maximum, but would oscillate between each consecutive turn. This is because the orbit is not well centered, and leads to a precession in the orbit.

3.2.1 Finding an initial position

The matched distribution finder in OPAL was used to find an initial starting radius and radial momentum for a single particle. With these values the particle was injected and simulated during a few turns without any acceleration to confirm that the orbit was closed. However, the inititial position and radial momentum is different for a closed orbit and an accelerated orbit at lower energies. This is because the accelerated orbit is not centered around the cyclotron's center point due to the radial kicks from the RF cavities. As the kinetic energy increases, the difference between the accelerated and closed orbits decreases when the RF cavity kicks becomes less and less important compared to the radius and energy of the accelerated orbit. The correct initial conditions were found by creating a 2D grid with a number of simulations varying the radius r and radial momentum p_r in steps. In order to measure the effect of varying r and p_r, each simulation was labelled by the amplitude of the oscillations in the turn-to-turn separation: after the first 20 turns, when the turn-to-separation is larger than in the rest of the simulation, define the the amplitude as:

$$A(r, p_r) = \frac{\max TS_{\{r,p_r\}}}{\min TS_{\{r,p_r\}}} - 1, \tag{3.1}$$

where TS designates the turn-to-turn separation. The amplitude is at a minimum when $\max TS_{\{r,p_r\}} \approx \min TS_{\{r,p_r\}}$. By mapping out the space $(r, p_r, A(r, p_r))$ we can obtain a gradient and eventually find a local minimum corresponding to a well matched orbit.

3.2.2 RF phase

When the single particle crosses an accelerating gap, the phase at which it enters it relative to the RF phase of the cavity is recorded by OPAL. At zero phase, the particle would arrive exactly at the peak of the accelerating RF wave and be maximally accelerated. The RF phase needed to be transfered between the central and the outer region simulations in order to realistically restart the simulation. Because the particle injected by the spiral inflector travels some additional distance before entering the first RF cavity an initial phase offset of the RF cavities must be given such that the two simulations agree. This was done by comparing the RF phase as given by the OPAL output files between the different simulations. The original orbit was used as a reference for the spiral inflector orbit, and by shifting the initial RF phase for the spiral inflector orbit these were matched. Afterwards the RF phase offset of the restarted orbit was also matched to the original orbit.

3.3 Multi particle simulations

3.3.1 Initial particle distribution

Having found an accelerated orbit for a single particle starting just after the electrostatic spiral inflector the next goal was to accelerate a single bunch through the cyclotron. The bunch is injected with a beam size σ_x, momentum spread σ_{px}, position-momentum correlations $CORRX$ in each plane , and correlations between the momentum and beam size in the radial and longitudinal planes: $R51$, $R52$, $R61$, and $R62$. These values are defined by their position in the sigma matrix:

$$\begin{pmatrix} \sigma_x^2 & CORRX\sigma_x\sigma_{px} & 0 & 0 & R51\sigma_x\sigma_y & R61\sigma_x\sigma_{py} \\ CORRX\sigma_x\sigma_{px} & \sigma_{px}^2 & 0 & 0 & R52\sigma_{px}\sigma_y & R62\sigma_{px}\sigma_{py} \\ 0 & 0 & \sigma_z^2 & CORRZ\sigma_z\sigma_{pz} & 0 & 0 \\ 0 & 0 & CORRZ\sigma_z\sigma_{pz} & \sigma_{pz}^2 & 0 & 0 \\ R51\sigma_x\sigma_y & R52\sigma_{px}\sigma_y & 0 & 0 & \sigma_y^2 & CORRY\sigma_y\sigma_{py} \\ R61\sigma_x\sigma_{py} & R62\sigma_{px}\sigma_{py} & 0 & 0 & CORRY\sigma_y\sigma_{py} & \sigma_{py}^2. \end{pmatrix}$$

In OPAL, the bunch is initiated using a Monte Carlo random number generator that creates a given number of particles with a Gaussian distribution according to the sigma matrix. If a matched distribution is found, the internal forces of the beam (i.e. space charge) would be balanced out by the external forces of the focusing magnets and the beam would undergo periodical rotations. A mismatched beam can fragment into secondary bunches or completely blow up inside the machine. An initial guess for the second order moments is provided by the matched distribution finder integrated in OPAL. However, the matched distribution does not take into account nonlinear space charge or the RF kicks on the beam. Therefore, the initial guess was modified by minimizing the beam's maximum root mean square (RMS) in each dimensions while varying the initial RMS sizes $(\sigma_x, \sigma_y, \sigma_z)$. All other parameters, e.g. the momentum spreads and momentum-position correlations were taken from the matched distribution finder.

3.3.2 Design parameters and quantities of interest

The design of the beam in a cyclotron is a multi-objective optimization process where several goals must be met simultaneously. For example, the injected beam should be realistic to produce, have low losses, and be safely extracted at the final turn in the cyclotron. The radial, longitudinal, and vertical root-mean-square values define the three half-axes of an ellipsoid within which 68% of the bunch particles are contained. This was used to analyze the dynamics of the beam core, i.e. when the beam core is matched, the RMS sizes stay should stay constant. However, we will also need to consider the outer particles of the bunch, because they will represent most of the beam losses in the cyclotron. This was done using a modified form of the bunch's fourth order moment, known as the halo parameter. The halo parameter describes the tailedness of a distribution, and the higher it is, the longer and higher are the tails of the distribution. The halo parameter is the normalised fourth order moment subtracted by 1, and a perfect Gaussian beam would have a halo parameter value of 1. So in order to have matched beam core and a minimal beam halo to minimize losses, the RMS sizes in each direction should be kept as low as possible and the halo parameter as close to 1 as possible. Finally, the projected emittance of a beam is defined as the area in the (x, p_x) space, known as the phase space, within which 68% of the particles in those coordinates are contained. In this way, the emittance is a measure both of the energy spread and the spatial spread of the particles. The emittances should stay constant for a matched beam, but growth or loss of emittance could occur if there is strong coupling between the different planes. Since the emittance decrease with increasing energy, the normalised emittance is used which is independent of energy.

Definition 1. *Root mean square (RMS) beam size*

$$RMS = \sqrt{\langle x^2 \rangle} \tag{3.2}$$

Definition 2. *Halo parameter (H) [21]*

$$H = \frac{\langle x^4 \rangle}{\langle x^2 \rangle^2} - 1 \tag{3.3}$$

Definition 3. *Emittance (ϵ) [22]*

$$\epsilon = \sqrt{\langle x^2 \rangle \langle x'^2 \rangle - \langle x \rangle \langle x' \rangle} \tag{3.4}$$

Definition 4. *Normalised emittance (ϵ_N) [22]*

$$\epsilon_N = \beta\gamma\epsilon \tag{3.5}$$

3.3.3 Collimators

In order to cut the beam halo from the outer part of the bunch, radial collimators were placed around the beam orbit at different locations, 45 degrees apart. A number of simulations were performed with collimators placed after turns $6, 7, 8, 9$, or 10. The collimators were identical blocks that were placed radially below and above the orbit. The simulations were performed as a proof-of-principle of the collimation scheme, and does not represent a realistic design from an engineering point of view.

4 Results

4.1 Initial position

In order to determine the optimal initial conditions for a single particle orbit, the turn separation amplitude was plotted in figure 4.1 (a) as a function of initial radius and radial momentum with a fixed energy of 193.7 keV/amu. The dark blue areas corresponds to initial radii and radial momentums that gives a well-centered orbit, and the initial parameters corresponding to the minimal amplitude was plotted in 4.1 (b). This was given by an initial radius of 117.9 mm, a radial momentum of 0.0023 $\beta\gamma$ and initial RF phase offset of 281 degrees.

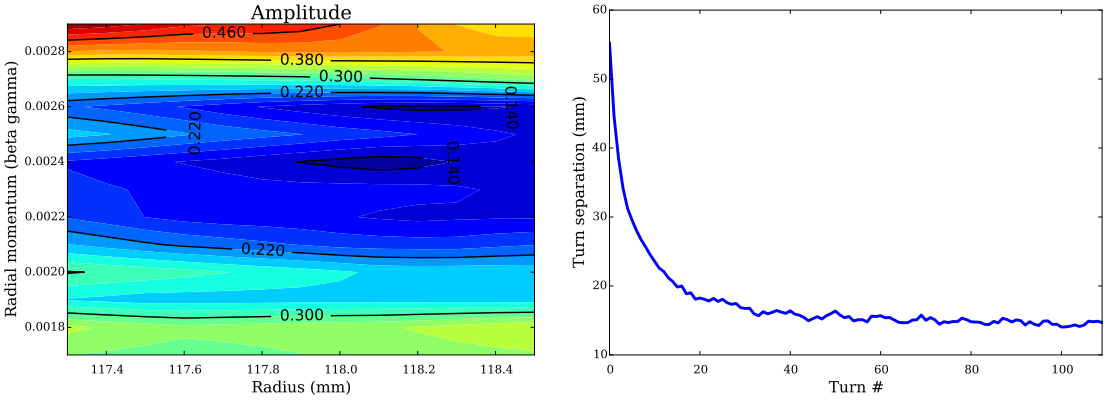

(a) Amplitude of the turn-to-turn separation as a function of initial radius and radial momentum.

(b) Turn-to-turn separation of the orbit

Figure 4.1: Plot of the amplitude of the turn-to-turn separation as a function of initial position and momentum. The deep blue regions in the left plot corresponds to the local minima in the amplitude, which is a well-centered orbits, with its turn-to-turn separation plotted on the right. An orbit with a high amplitude in its turn-to-turn separation corresponds to a mismatched beam as its trajectory would oscillate in the horizontal plane, so the amplitude should be minimized in order to find a matched orbit.

4.2 Tunes

Figure 4.2 shows the tune diagram of the radial ν_r and vertical ν_z tunes, starting from 0.5 MeV/amu. The tunes for the first turns are not plotted as they were far away from the others, and because the beam quickly leaves the central region so that the problem with resonances is smaller in the centre. We see from the figure that the most dangerous resonances of $\nu_r = 1$ and $\nu_z = 0.5$ are avoided since the beam passes through them quickly. The $\nu_v = \frac{2}{3}\nu_r$ and $\nu_v = \frac{2}{3}$ resonances pose potential problems but are weaker resonances.

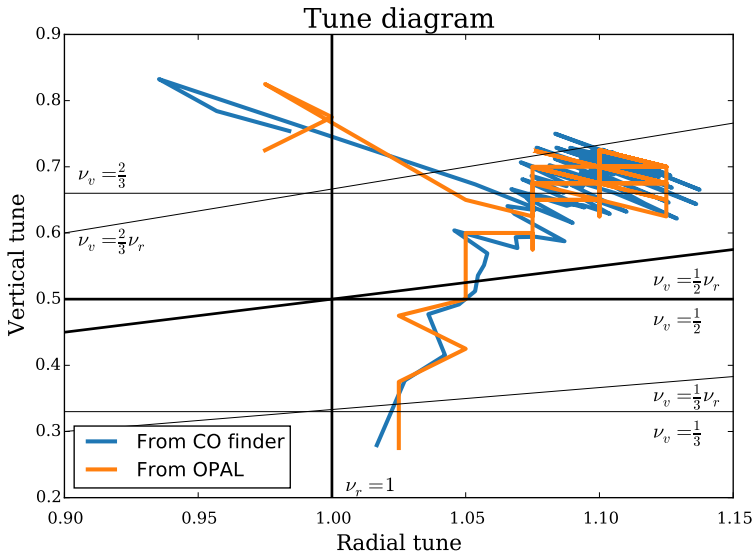

Figure 4.2: Tune diagram of the cyclotron comparing the two particle tune calculation mode in OPAL and the tune calculated by the closed orbit finder. The thick black lines corresponds to strong resonances and the thin black lines to weaker resonances.

4.3 Injection

In figure 4.3 the complete orbit for a single particle, from injection through the spiral inflector and through the full cyclotron field map is plotted. The orbit is a combination of the simulations for the central region and outer region. The vertical oscillations of the same orbit are plotted in figure 4.4. In figure 4.5 the RF phase slip of a single particle can be seen. Towards the end the particle loses isochronicity, which causes it to arrive at a slightly lower phase for each subsequent turn. In order to get these results, the electric field strength of the spiral inflector had to be scaled up by a factor of 1.036 and the injection energy had to be decreased from 70 keV to 64 keV compared to the original design of the spiral inflector. The side view of the "scaled" particle trajectory in the injection region is plotted in figure 4.6 together with the trajectory of a particle with an injection energy of 70 keV and an electric field scaling of 1.0.

4.4 Initial particle distribution

The initial particle distribution at 193.7 keV/amu used the initial coordinates r, pr for the centroid as obtained by the single particle tracking. To get an estimate of how well matched the beam was, different initial distributions in the radial-longitudinal planes, with the vertical initial beam size kept constant, were plotted against the maximal RMS beam size attained after tracking for 15 turns. This is shown in figure 4.7. As would be expected, decreasing the initial RMS size of the beam in the radial-vertical directions lead to an increase in the vertical direction as the vertical focusing is very weak in the first turns. A solution was therefore chosen such that the beam would be well matched in the radial-longitudinal plane without blowing up in the vertical direction. To mitigate the increase in vertical bunch size the effect of starting with a converging

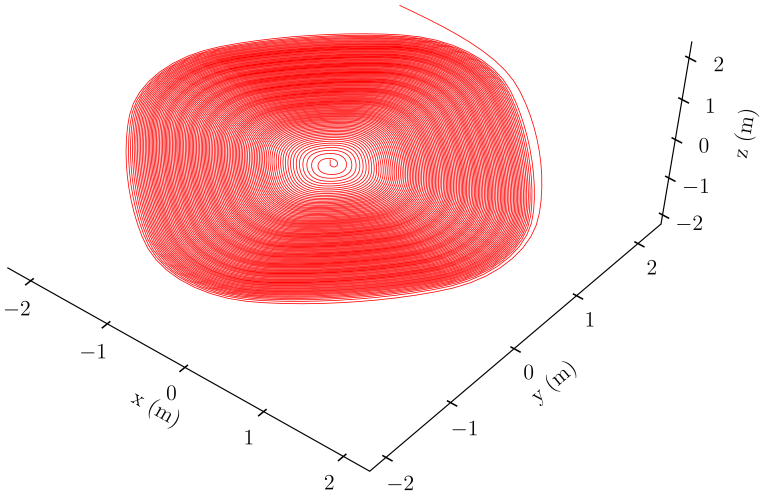

Figure 4.3: 3D plot of a single particle injected through the spiral inflector and subsequentially accelerated through the cyclotron.

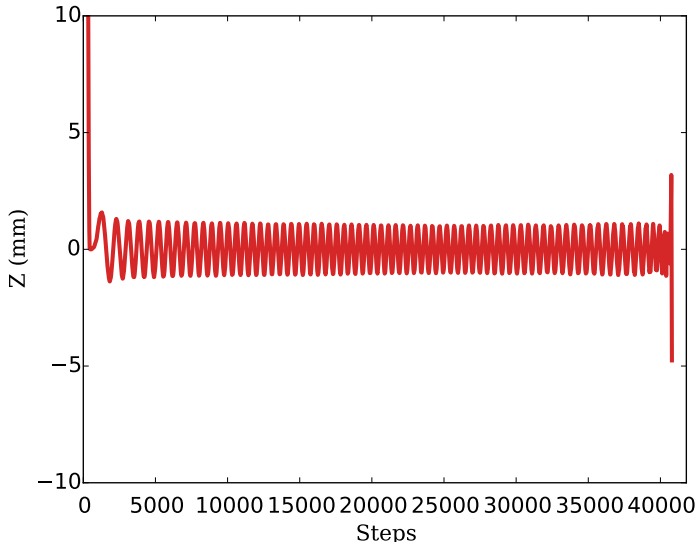

Figure 4.4: Side view of the single particle orbit. The particle comes in slightly off-centered which results in an oscillation around the midplane.

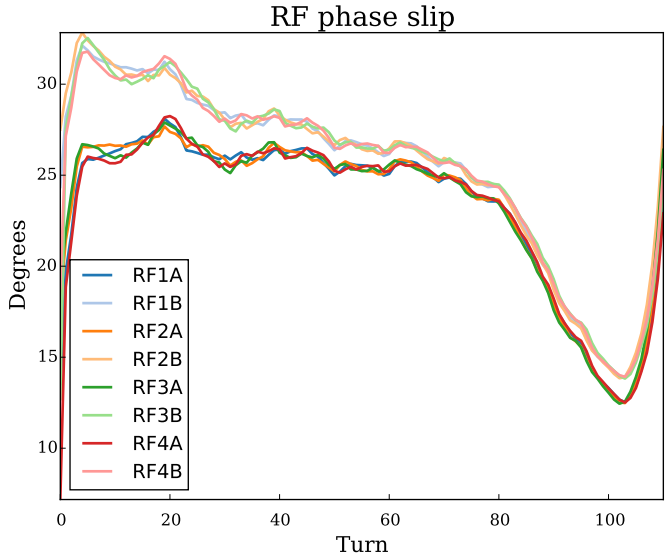

Figure 4.5: RF phase slip for a single particle with respect to each cavity gap in the cyclotron. A phase slip of 0 means that the particle comes in at the peak of the RF accelerating wave and is being maximally accelerated.

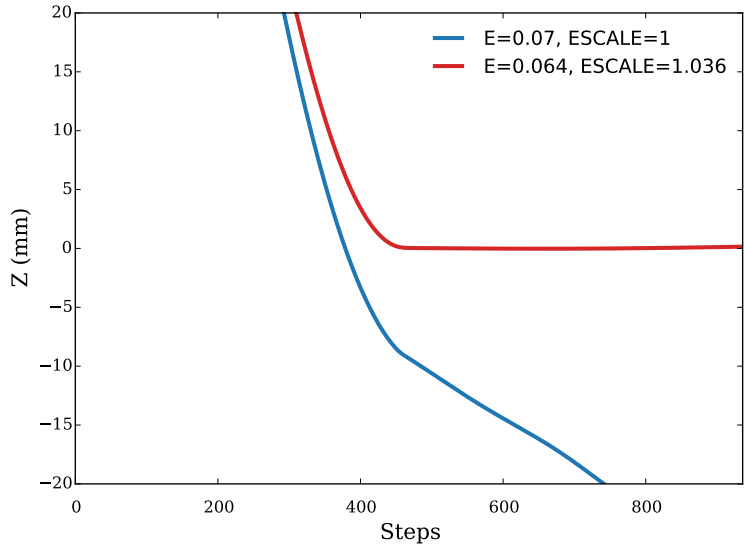

Figure 4.6: Scaling of the spiral inflector electric field

beam was also considered. The results in figure 4.8 for different convergence rates show that a converging beam can be used to contain the maximum vertical extent attained, but that the effect is limited to $\approx 10\%$ compared to having no convergence at all.

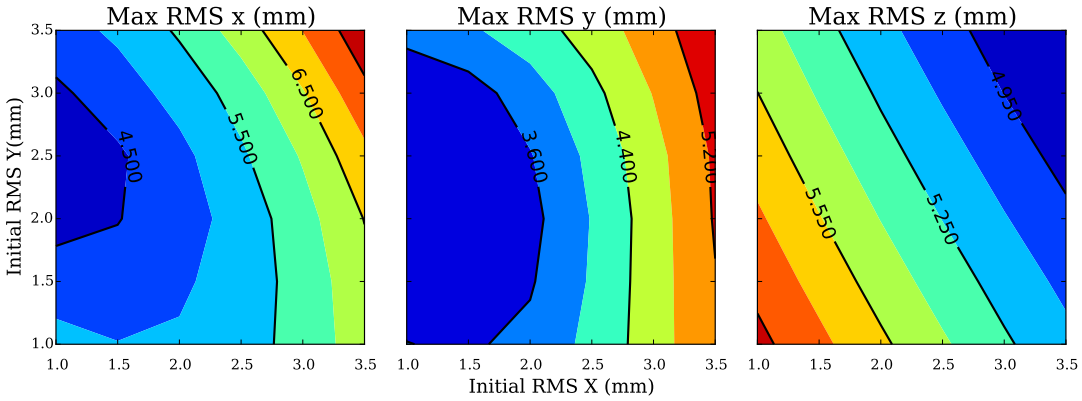

Figure 4.7: Landscape of the maximum RMS size in x, y, and z-directions after first 15 turns. The deep blue regions corresponds to the lowest maximum RMS beam size, and therefore the best matched configuration.

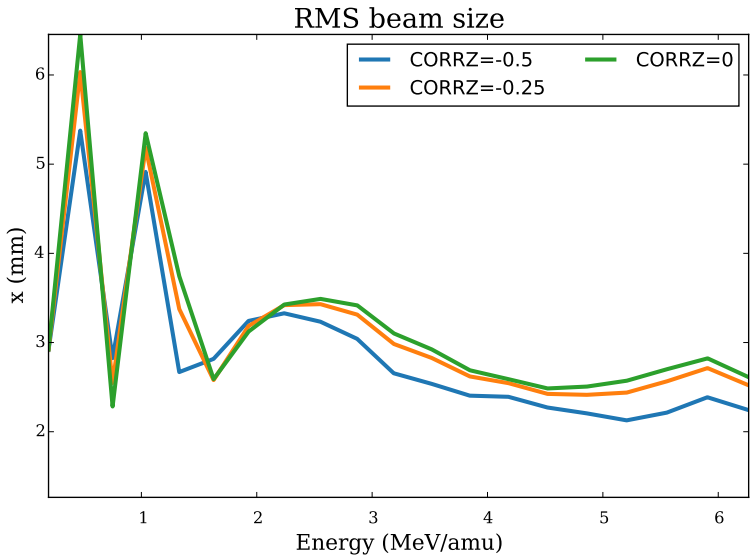

Figure 4.8: Correlation of z-pz. The higher the negative correlation, the more the beam is converging in that plane.

4.5 Collimation

In order to determine the optimal placement of the collimators, a set of simulations were run where the collimators were placed after turn $6, 7, 8, 9$, and 10, respectively. The beam was injected with a beam current of of 6.65 mA and with a collimator gap width of 16 mm, 5.1 mA survived after collimation. The beam RMS sizes for each of the collimation schemes is shown in figure 4.12, the projected emittance in 4.11, and the halo parameter in 4.13. While there is a clear effect on the RMS size and the projected emittance, the shapes are more or less identical and the peak values vary only slightly. This shows that the bunch core size and emittance is not strongly dependent of the collimation, which is expected since the collimators cut in the outer parts of the beam. Generally, placing the collimators after turn 6 seems to give rise to the smallest RMS growth in the vertical and longitudinal directions, while turn 8 sees a bigger RMS growth. However, we can see from the halo parameter in 4.13 that placing the collimators too early, after turns 6 or 7, can yield a much larger halo growth than placing the collimators after turns $8 - 10$. Placing the collimators too late also led to an increase in the longitudinal and radial halo parameters, and the optimal collimator placement with respect to the halo parameter is after turn number 8. Figure 4.10 shows the orbit of the centroid of the bunch up to the maximal energy of 60 MeV/amu, with a set of collimators placed after turn 10. This shows that the initial conditions given by the single particle study gave stable results, even for a multi-particle bunch. As is seen in the plot, the centroid of the bunch shifts due to the large influence of the beam halo in the first turns. After the collimators the halo is cut from the beam and the discrete jumbs of the centroid are no longer seen.

To visualize the beam dynamics during the first few turns, the (x, y) and (x, p_x) projections of the beam in the first 12 turns are plotted in figures 4.14 and 4.15. The beam is initially mismatched, but the beam core develops a matched distribution in the first $6 - 8$ turns while the beam halo is initially growing and contains about 5% of the particles. After cutting the halo, a

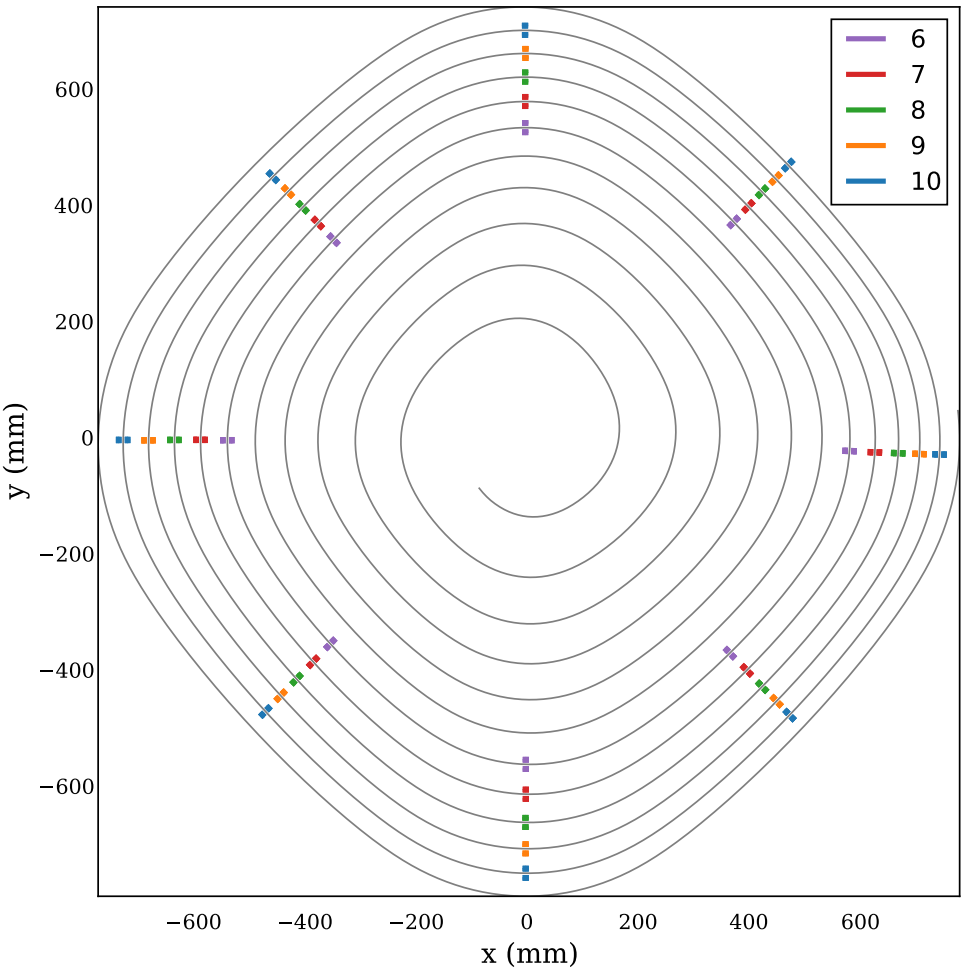

Figure 4.9: Placement of the collimators during turn $6, 7, 8, 9$, and 10 in the cyclotron.

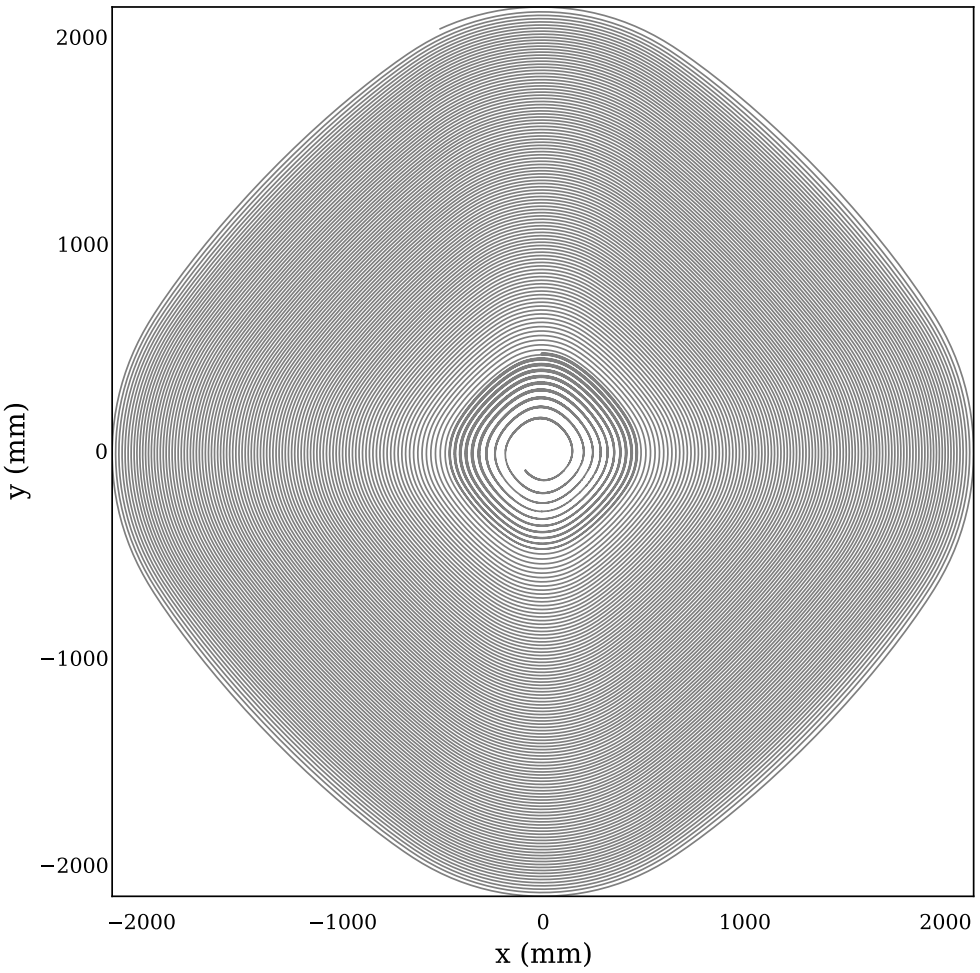

Figure 4.10: Top view of the bunch orbit, starting at an azimuthal angle of −135 degrees in the first turn after injection.

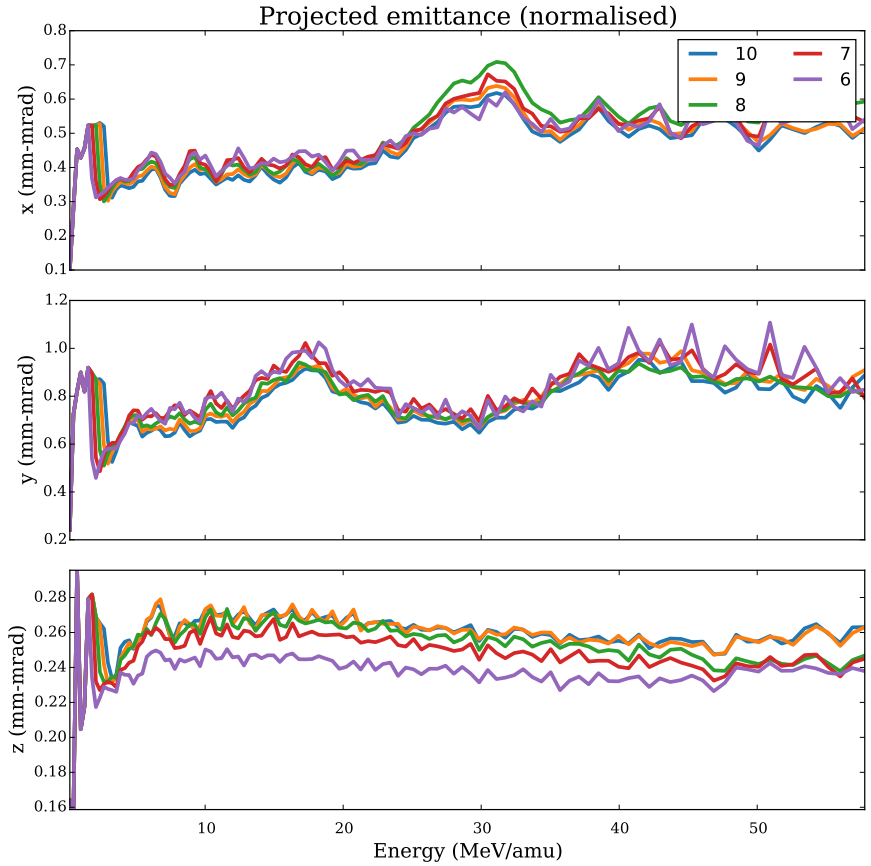

Figure 4.11: Emittance growth as a function of various collimator placements.

nearly Gaussian beam seems to have developed at turn 12. We see a similar effect in figure 4.14 for the (x, p_x) phase space, but note that there are still outlying particles.

4.6 RF phase offset

A similar set of experiments was performed where the initial RF phase offset of the RF cavities was varied in steps of 10 degrees, from 271 to 291 degrees. A higher phase shift means that the particles come in closer to the accelerating crest of the RF cavity, as can be seen in figure 4.16. The initial RF phase offset was taken from the single particle trajectory. These results are shown in figures 4.19, 4.17, and 4.18, showing the RMS beam size, emittance, and halo parameter. In figure 4.17 we see that running with a higher phase shift leads to an increase in vertical and longitudinal projected emittances, and to a decrease in the vertical projected emittance relative to a phase offset of 271 degrees. Since only the total emittance is conserved, and not the emittances projected on the different phase spaces, it is not suprising that the emittance is oscillating. In figure 4.18 the halo parameter is shown and it can be seen that for an offset of 271 degrees, a larger halo develops in the radial and longitudinal directions while it develops a smaller halo in the vertical direction. In figure 4.19 we see that the lowest beam size growth in

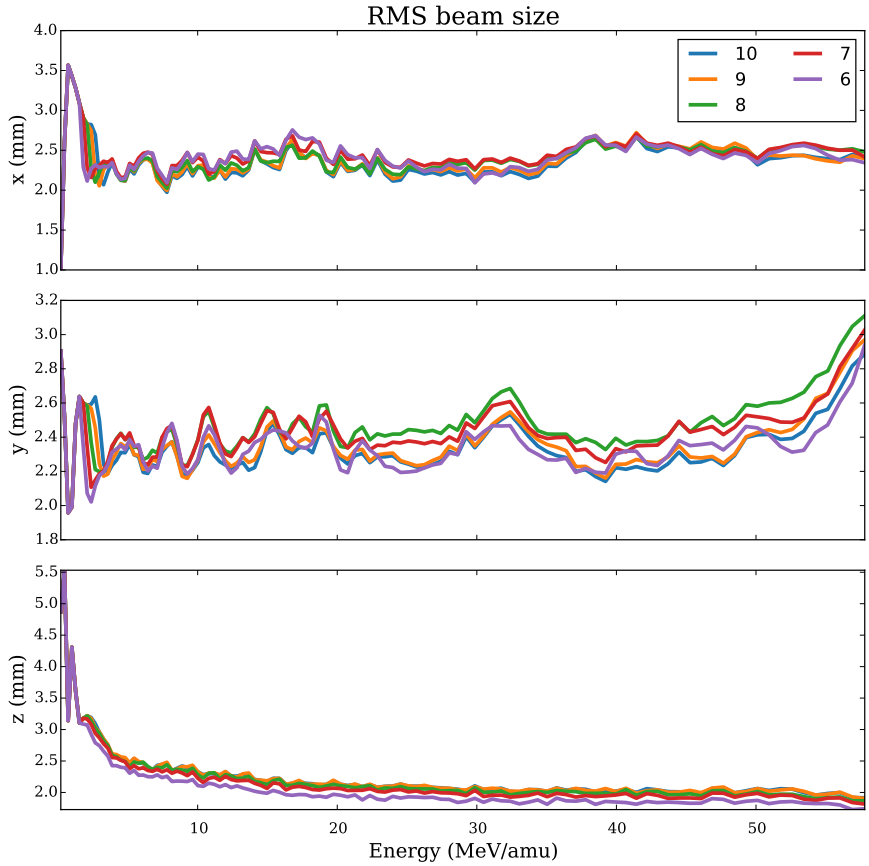

Figure 4.12: RMS growth as a function of various collimator placements.

radial and longitudinal directions occurs for the lowest phase shift of 271 degrees. It is important to note that since the orbit depends on energy, the collimators are located at different radii and cut the beam at different energies, which also has an impact on the results. In a full study, the RF phase offset and collimator placement has to be varied simultaneously since they are dependent on each other.

4.7 Extraction

As is seen in figure 4.1 (b), the turn separation at the final turn for a single particle is close to 15 mm, which is in good agreement with the theoretical calculations of 14.7 mm. During the last few turns of the trajectory, the beam passes through a number of beam probes that records the position at the passing of each particle without destroying it. This allows to measure the bunch separation and plot number of particles as a function of their radius, which is shown in the histogram in figure 4.20. The bunch peaks are also separated by about 15 mm, but there is a significant halo overlap which is more clearly seen in 4.21. This means that the radiation damage on the septum is probably too high, but this result could be significantly improved by introducing a $\nu = 1$ resonance or by injecting the beam slightly off-centered to get a increase in

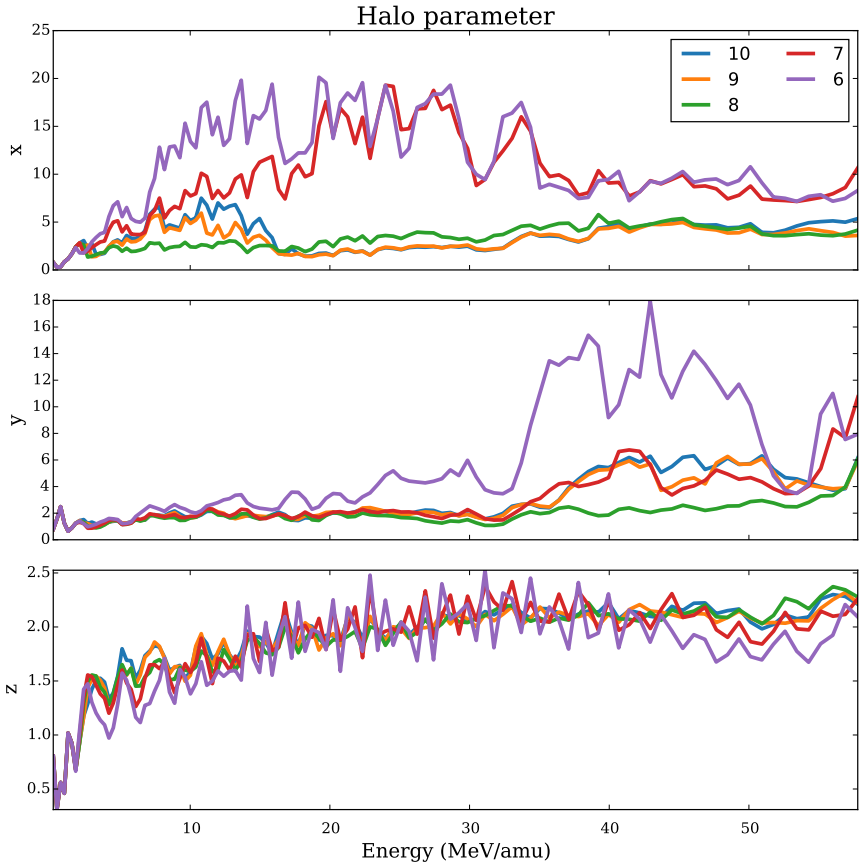

Figure 4.13: Halo growth as a function of various collimator placements.

turn separation from precessional motion.

h]

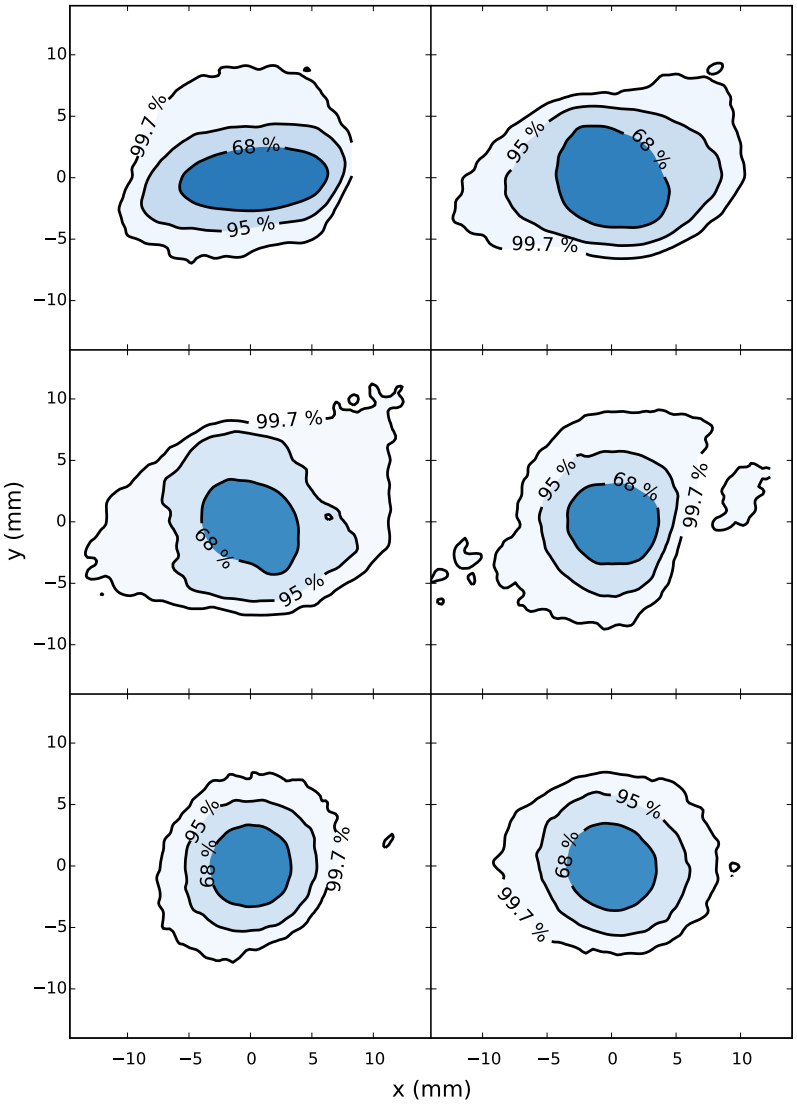

Figure 4.14: Snapshots of the beam in x-y plane during the turns $2, 4, 6, 8, 10$, and 12, from left to right, top to bottom. The numbers show the percentage of the beam enclosed within the contour.

Table 4.1: Overview of the results from the IsoDAR simulations

Parameter	Thesis	Yang [4]	Units
E_{kin}	193.7	534	keV/amu
I_{init}	6.65	5.0	mA
I_{final}	5.1	5.0	mA
r	117.9	191.8	m
p_r	0.0023	$1.56e-3$	$\beta\gamma$
$\epsilon_{N,x}$	0.132	25.6	mm - mrad
$\epsilon_{N,y}$	0.241	5.35	mm - mrad
$\epsilon_{N,z}$	0.558	25.6	mm - mrad
$RMSx$	1.0	0.84	mm
$RMSy$	3.0	0.93	mm
$RMSz$	5.0	1.85	mm
$RMSp_x$	$1.34e-4$	$1.77e-4$	$\beta\gamma$
$RMSp_y$	$8.49e-5$	$3.38e-5$	$\beta\gamma$
$RMSp_z$	$1.18e-4$	$8.11e-5$	$\beta\gamma$
$CORRX$	$-2.16e-3$	0	
$CORRY$	$3.61e-3$	0	
$CORRZ$	$-8.36e-05$	0	
$R61$	0.693	0	
$R62$	$-8.29e-4$	0	
$R51$	$-7.28e-4$	0	
$R52$	0.7025	0	
Collimators	8	4	
Phase offset	271	-2	degrees
Initial angle	225	45	degrees

4.8 Parameters and sigma matrices

The final simulation parameters that were used are shown in table 4.1 in comparison with the values used in the previous simulation [4].

The initial sigma matrix that gave the optimal matched distribution was determined to be, in units of m and $\beta\gamma$:

$$\begin{pmatrix} 1e-6 & -6.90e-17 & 0 & 0 & -6.55e-15 & 7.90e-16 \\ -6.90e-17 & 3.2e-8 & 0 & 0 & 2.023e-13 & -3.41e-20 \\ 0 & 0 & 9.67e-6 & 2.3e-16 & 0 & 0 \\ 0 & 0 & 2.3e-16 & 6.6e-9 & 0 & 0 \\ -6.55e-15 & 2.023e-13 & 0 & 0 & 9e-6 & -5.42e-18 \\ 7.90e-16 & -3.41e-20 & 0 & 0 & -5.42e-18 & 7.21e-9 \end{pmatrix}$$

The sigma matrix corresponding to the values obtained from Yang is [4]

$$\begin{pmatrix} 6.4e-07 & 0 & 0 & 0 & 0 & 0 \\ 0 & 3.13e-8 & 0 & 0 & 0 & 0 \\ 0 & 0 & 8.65e-7 & 0 & 0 & 0 \\ 0 & 0 & 0 & 1.14e-9 & 0 & 0 \\ 0 & 0 & 0 & 0 & 3.42e-6 & 0 \\ 0 & 0 & 0 & 0 & 0 & 6.58e-9 \end{pmatrix}$$

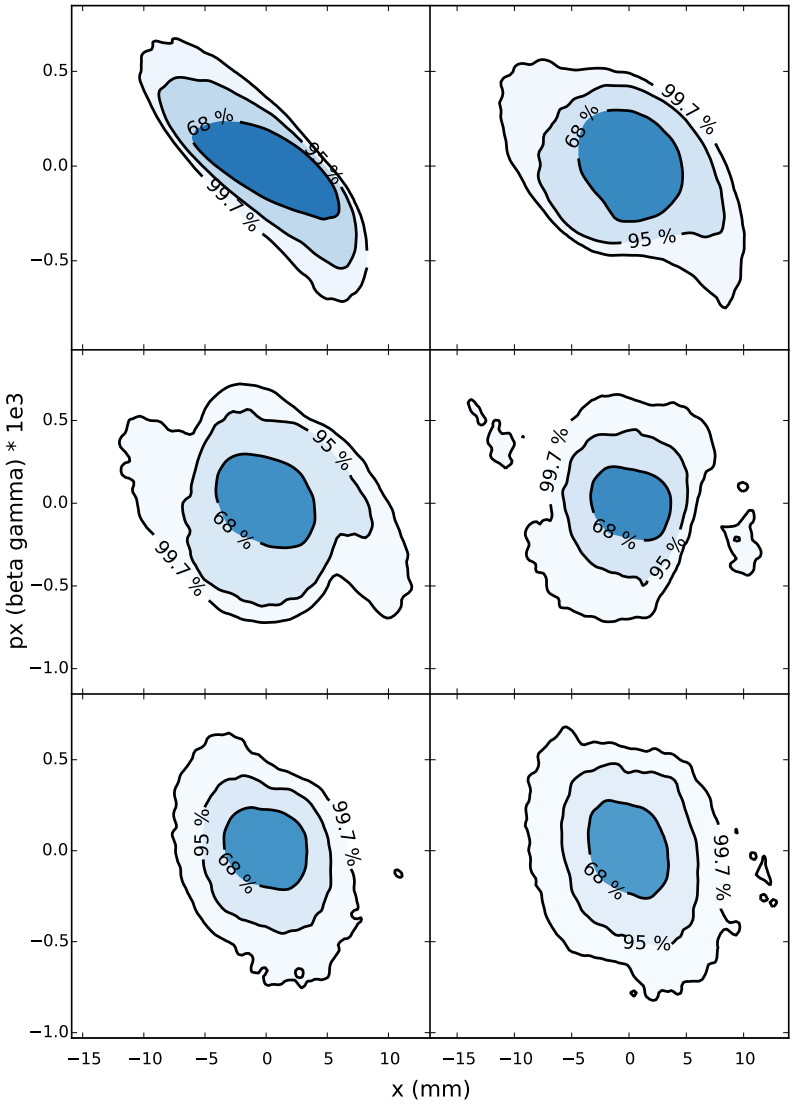

Figure 4.15: Phase space snapshots of the beam in the x-px plane during the first 12 turns. The numbers show the percentage of the beam enclosed within the contour.

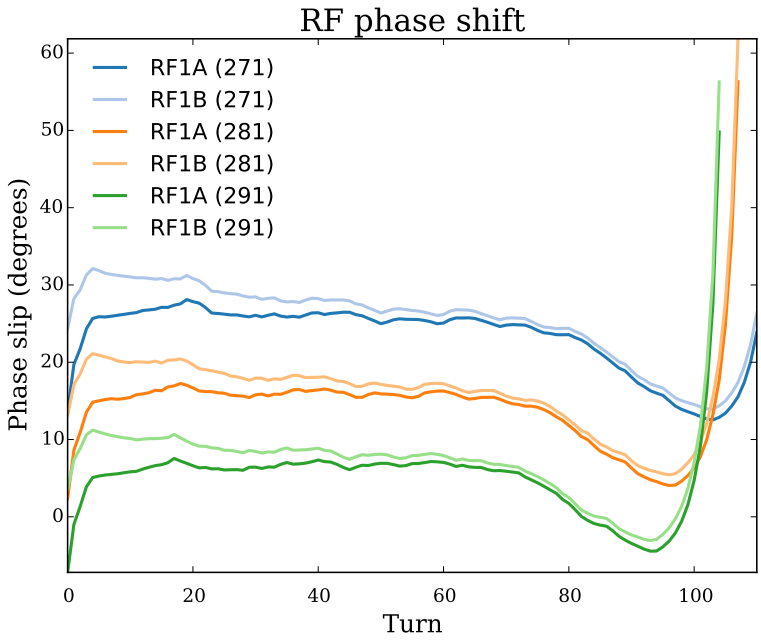

Figure 4.16: RF phase slip for different initial cavity phase offsets.

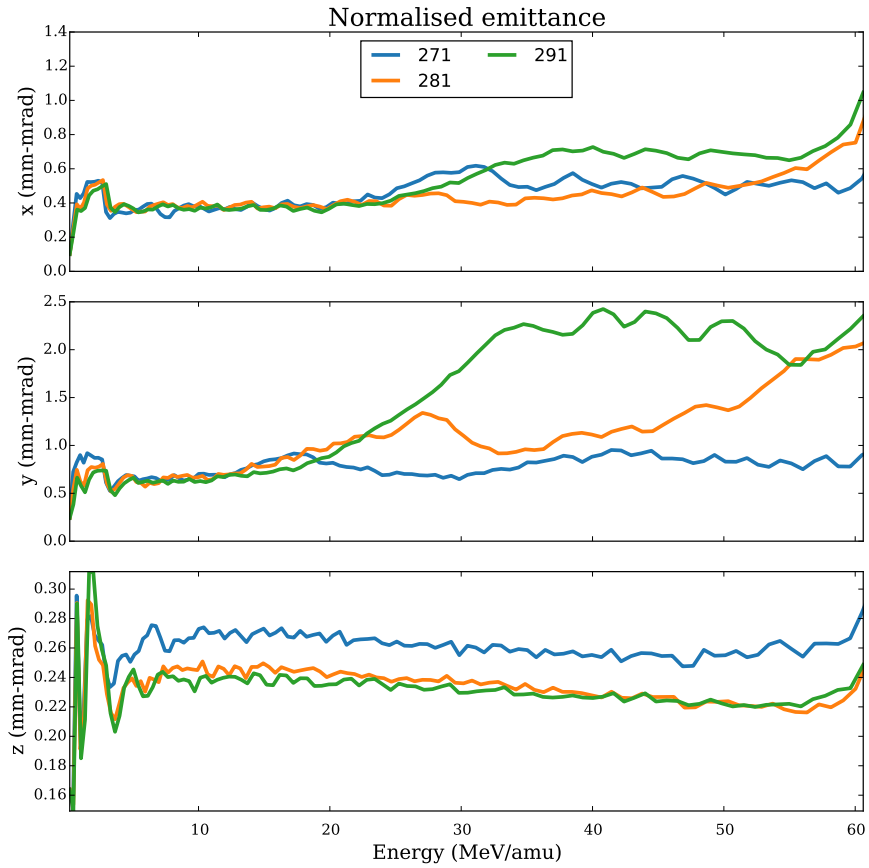

Figure 4.17: Projected emittance growth as a function of RF phase.

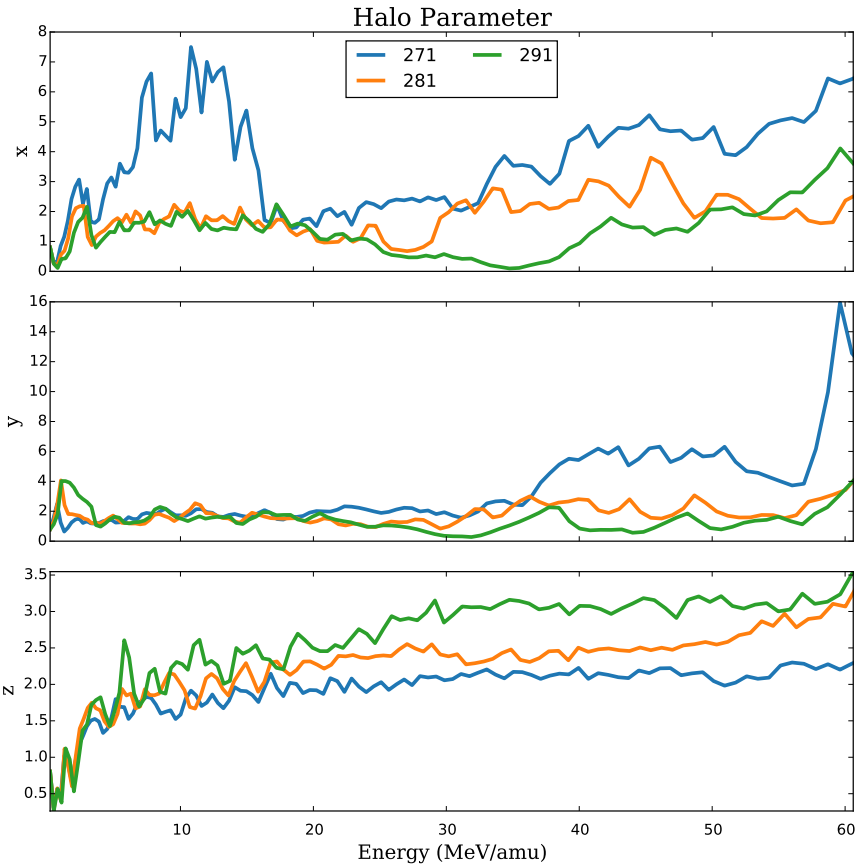

Figure 4.18: Halo growth as a function of RF phase.

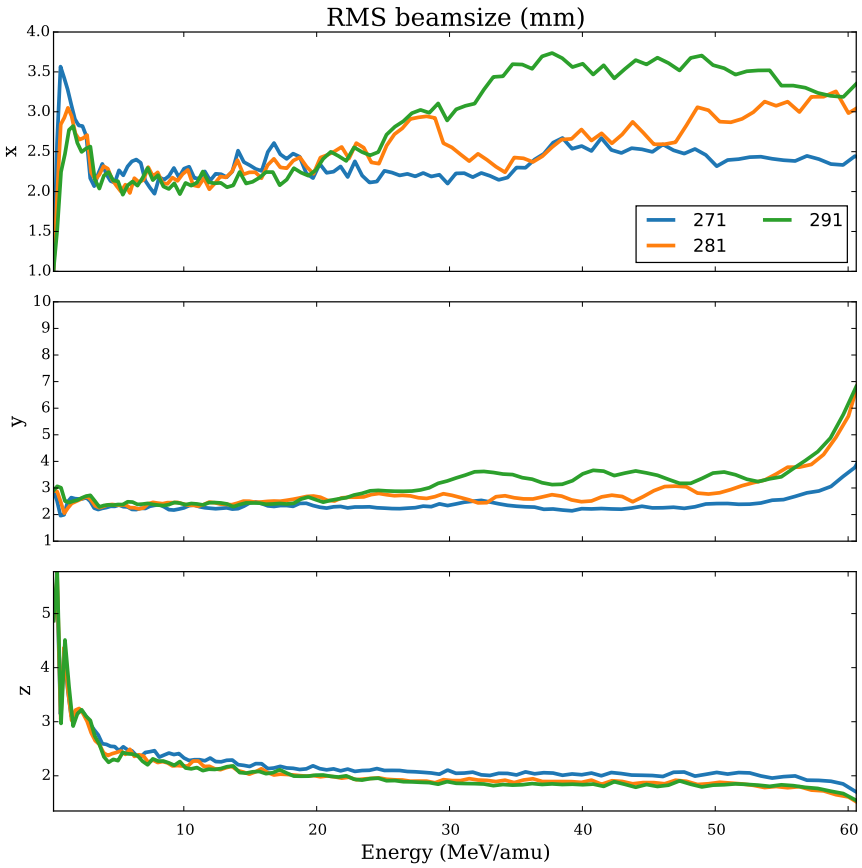

Figure 4.19: RMS growth as a function of RF phase.

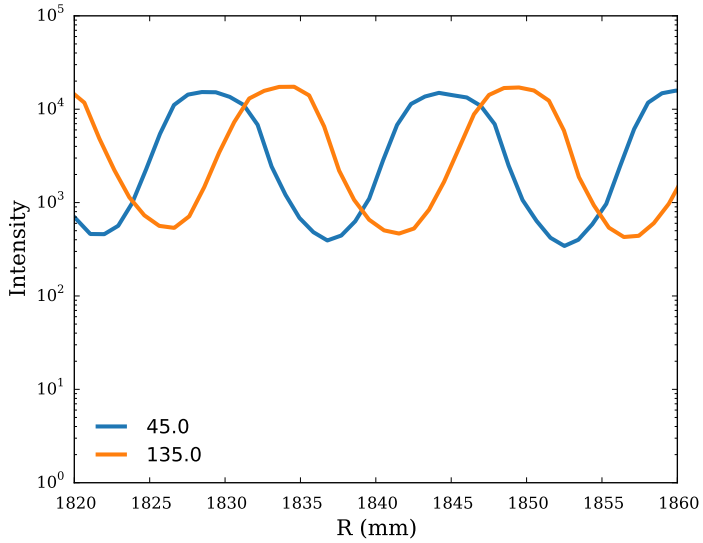

Figure 4.20: Histogram of the bunch distribution in the radial-vertical plane during the last few turns in the accelerator. The numbers indicate the angle at which the distribution is measured.

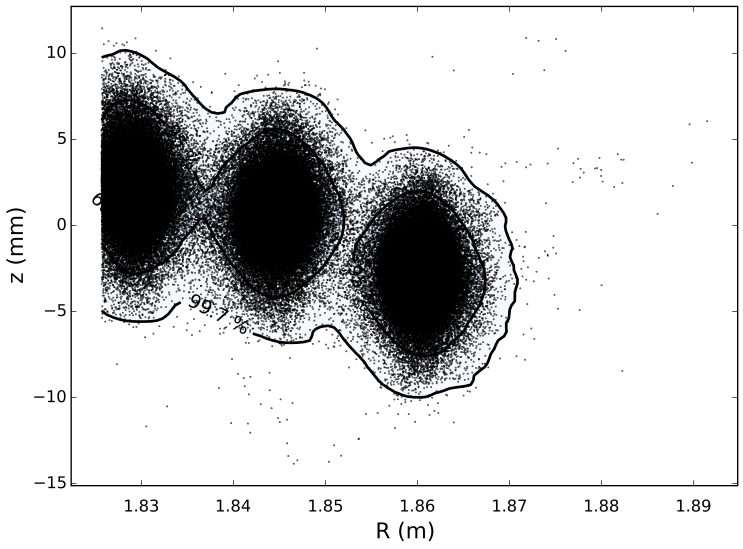

Figure 4.21: The two last turns projected on the $R - z$ plane, at an azimuthal angle of 315 degrees in the cyclotron.

5 Discussion

The compact cyclotron described in this thesis is a versatile particle accelerator to be used as a high-intensity proton driver for the IsoDAR sterile neutrino experiment, and later as an injector cyclotron into the superconducting ring cyclotron for the DAEδALUS neutrino CP-violation experiment. One of the main challenges for both projects is to achieve a high intensity neutrino beam to measure the neutrino oscillation with a high statistical certainty. The IsoDAR cyclotron can provide 10 mA beam current on target with an energy of 60 MeV/amu, and combined with the DAEδALUS superconducting cyclotron an energy of 800 MeV/amu can be reached. A beam current this high has never been achieved before and would be an important breakthrough in the field of accelerator physics. The main advantage of the IsoDAR cyclotron is the use of H_2^+ ions instead of protons which means that the total beam current on target can be doubled while minimizing space charge. In the DAEδALUS cyclotron, the use of H_2^+ also provides an efficient extraction mechanism through foil stripping to produce ions of higher charge that would be bent more in the magnetic field. An efficient design of the compact cyclotron requires high-fidelity simulations of the beam to ensure that important design goals are met, such as a large turn separation at extraction and low losses in the cyclotron. In this thesis, the beam dynamics of a high-intensity bunch travelling in the cyclotron was simulated in the OPAL particle accelerator code. The simulation was started at an energy of 193.7 keV/amu in the central region of the cyclotron. The simulations showed that the IsoDAR cyclotron is capable of maintaining the high intensity particle bunch as a matched distribution developed in the cyclotron given the right initial conditions on the beam. The bunch could then be transported trough the machine up to the extraction energy while maintaining a turn separation of 15 mm to minimize the influence of neighbouring bunches, and to enable an efficient extraction. By placing a set of collimators during one turn in the cyclotron and adjusting the initial phase offset of the RF cavities the beam halo that developed in the first turns was minimized. The beam was injected with a current of 6.65 mA, and after collimation a current of 5.1 mA survived up to extraction. First simulations were also performed for the spiral inflector, which showed that the injection into the cyclotron is feasible with an injection energy of 35 keV/amu. A single particle was injected through the spiral inflector and its orbit could be matched with the cyclotron to yield a well-centered orbit up to the extaction energy. In order to simplify the simulations they were performed over a restricted parameter space, and the effects of the initial parameters on the beam was determined by using a number of quantities of interest. For the single particle simulations, the initial parameters were the radius, radial momentum, RF phase offset, and scaling of the spiral inflector electric field. The quantities of interest were the oscillation amplitude in the turn-to-turn separation and the final turn separation, where the former should be minimised and the latter maximised. In this thesis, the optimal parameters were obtained considering the only the minimisation of the turn-to-turn separation oscillation, and the final turn separation was left for future studies. The multi particle simulations used the optimum of the radius and radial momentum from the single particle simulations, and added a number of other parameters related to the distribution of the initial beam, as well as the placement of collimators in the cyclotron. The beam was initialised with a Gaussian distribution with couplings in the longitudinal-radial plane and a decoupled vertical plane. In total, 13 parameters determined the initial beam distribution; the initial RMS size σ_x and RMS momentum σ_{px}, the xp_x coupling terms $CORRX$ and the four coupling terms between the longitudinal and radial planes: $R51$, $R52$, $R61$ and $R62$. To find an initial guess for these parameters the matched distribution finder in OPAL was used, which produced the sigma

matrix given an initial beam emittance. The simulations were then performed by varying the initial spatial distributions and keeping the coupling terms from the matched distribution finder constant. The latter was only motivated by the fact that it simplified the simulations, and the influence of these parameters on the final result was not investigated. The quantities of interest for the multi particle simulations were chosen as the RMS beam size in each plane, the halo parameters, and the projected emittances, which all should be minimised by varying the initial parameters and the collimator placements.

The result of these simulations should be compared with the previous simulations performed by Yang [4], who performed his simulations with the major difference that his simulations started at the higher energy of 534 keV/amu compared to the simulations presented here, which started at 193.7 keV/amu. In his simulations, the horizontal, longitudinal, and vertical RMS beam sizes oscillate around 2.2, 2.7, and 2.0 mm, respectively, as can be seen in figure 1.5(b). In the simulations in this thesis, the values are similar: 2.5, 2.4, and 2.0, from figure 4.12. In Yang's paper the final turn separation, in figures 1.5(a) and 1.6(b), is large, with a distance of 20 mm between the final and next to final turns. The corresponding final turn separation achieved here, seen in figure 4.1(a), was lower, 15 mm, which would lead to higher radiation damages on the septum. This thesis, however, did not consider methods to increase the final turn separation such as introducing a first-order harmonic in the magnetic field map. We can also compare the initial parameters that were used in both simulations, seen in table 4.1. While the initial beam RMS sizes are comparable in the radial direction; 0.8 mm for Yang compared with 1.0 mm in this thesis, the difference is large in the longitudinal and vertical directions: 0.9 mm and 1.85 mm respectively for Yang and 3.0 mm and 5.0 mm here. The main reason for this is that the much lower focusing in the centre in addition to increased space charge due to the decrease in energy causes the beam to blow up in size. To get a matched distribution, the beam size therefore has to be increased in order to lower the charge density and decrease the defocusing space charge force.

5.1 Future outlook

In further studies of the beam dynamics of the IsoDAR cyclotron a number of issues should be addressed. First, it has to be shown that the beam can be injected within acceptable loss limits, which will mainly depend on the beam current that can be supplied from the ion source and radio frequency quadrupole located upstreams of the cyclotron. The final beam current, after injection losses and collimation, should be 5 mA and the difference between this and the maximum current that can be achieved will determine the maximum beam loss that can be tolerated. In order to achieve this, focusing elements has to be introduced before and after the spiral inflector to stop the beam from blowing up inside the cyclotron. The various electromagnetic fields acting on the beam in the central region of the cyclotron, e.g. the magnetic field from the bending magnets, the electrostatic field from the spiral inflector, the radiofrequency electric fields from the RF cavities and the magnetic or electric fields from the focusing elements has to be superimposed and studied in a full 3D model of the central region. The two main challenges in this study are to assure that the beam is vertically centered after injection, and that the vertical increase in beam size can be limited. Beam simulations, starting from the H_2^+ ion source, through the radiofrequency quadrupole and up to the spiral inflector should be performed to prove that the initial beam conditions can be met. When the injection has been simulated with a bunch and found to be feasible, a model cyclotron could be built to experimentally verify the simulation results.

Appendices

A Fieldmaps

The magnetic field map only covered 1/4th of the azimuth, and was extended automatically by OPAL assuming a rotational symmetry of 4. The matched distribution finder however only uses fieldmaps that cover a full 360 degrees. In order to accomodate for this, the fieldmap needed to be extended. The map has the following structure:

```
 0.000e+00
 1.000e+01
 0
 1.000e+00
    90
   251
    9.49392e+00    9.49392e+00    9.49392e+00    9.49392e+00    9.49392e+00
    9.49392e+00    9.49392e+00    9.49392e+00    9.49392e+00    9.49392e+00
    9.49392e+00    9.49392e+00    9.49392e+00    9.49392e+00    9.49392e+00
    9.49392e+00    9.49392e+00    9.49392e+00    9.49392e+00    9.49392e+00
    9.49392e+00    9.49392e+00    9.49392e+00    9.49392e+00    9.49392e+00
...
```

where the first row corresponds to the minimal radius $r_{\min}$, the radial step size Δr, the minimal azimuthal angle $\theta_{\min}$, the azimuthal angle step size $\Delta\theta$, the number of azimuthal steps N_θ, and the number of radial steps N_r. The values in the text body corresponds to the magnetic field strength B in units of kG. OPAL then reads the field map in the following way: from left to right, each value corresponds to the magnetic field strength $B(r, \theta)$, with theta being increased for each step $\theta = \theta_{\min} + N \cdot \Delta\theta$. As soon as the number of steps taken equals the number of azimuthal steps $N = N_\theta$, the radius is increased by Δr: $r = r_{\min} + \Delta_r$. In order to extend this field map, the blocks corresponding to a fixed radius r has to be repeated S times, where S is the symmetry factor. In the case for the IsoDAR, the symmetry factor is $S = \frac{360}{90} = 4$ and the number of rows that corresponds to a fixed radius is $\frac{90}{5} = 18$, where 5 is the number of columns. This means that each block of 18 rows should be copied 4 times, and the number of azimuthal steps should then be changed from 90 to 360. The full code for extending the field map, written in the scripting language Matlab:

```
% Works with CARBONCYCL type fieldmaps
clear all
Filename='Injmap20120405'; % Has to be a .dat file
data=importdata([Filename,'.dat'],' ',6);

% Read header
rmin = str2double(data.textdata(1));
deltar = str2double(data.textdata(2));
thetamin = str2double(data.textdata(3));
```

```
deltatheta = str2double(data.textdata(4));
Ntheta = str2double(data.textdata(5));
Nr = str2double(data.textdata(6));
[Nrows,Ncols] = size(data.data);
Theta = Ntheta*deltatheta;  % Angle covered by fieldmap
Sym_factor = 360/Theta;  % Symmetry of the fieldmap

N=Ntheta/Ncols; % Rows per radius step

A=data.data;
M=Sym_factor;
[~,n] = size(A);
% Creates matrix A2 which repeats all rows with the same fixed radius by the symmetry factor
A2 = reshape(kron(reshape(A',n*N,[]),ones(1,M)),n,[])';

fid=fopen([Filename,'_Symmetrized.dat'],'w');
fprintf(fid,[num2str(rmin),'\n']);
fprintf(fid,[num2str(deltar),'\n']);
fprintf(fid,[num2str(thetamin),'\n']);
fprintf(fid,[num2str(deltatheta),'\n']);
fprintf(fid,[num2str(Ntheta*Sym_factor),'\n']);
fprintf(fid,[num2str(Nr),'\n']);
fclose(fid);
str=[Filename,'_Symmetrized.dat'];
save(str,'A2','-ASCII','-append')
```

B Quick start guide

B.1 Build versions

OPAL version 1.5.00.1
Python 2.7.10
ROOT version 5.34.34

B.2 runOPAL

runOPAL.py is a python script that is used to start OPAL runs either on a computing cluster or on the local machine. It is used in the following way:

```
runOPAL.py VARIABLE=START:STOP:STEPSIZE --nobatch --test
```

where VARIABLE is a quantity to scan over, –nobatch tells OPAL to run the job on the local machine, and –test to only set up the folders and not submitting the jobs. Before a simulation is started, four things are needed in the simulation folder: an environment setup file, a template file, a fieldmap folder, and a .data file. The template file should be located in a subfolder with the name tmpl and have the file ending .tmpl. It has the same form as a regular OPAL input file except that the variables are replaced by VARIABLE:

```
pr0=_PR0_;
radius=_RINIT_;
angle=_THETA_;
```

and the values for these variables should be saved in the .data file:

```
PR0 0.0023
RINIT 117.9
THETA 0.0
```

To set the environment variables, typ source setup.sh in the terminal. When starting simulations for the first time, it is important to change the setup.sh file so that it points to the correct fieldmaps folder. The fieldmap can have different structures depending on the type of fieldmap. For the magnetic field map used in this simulation, see the appendix Fieldmaps.

B.3 The H5 format

In OPAL, most of the simulation results are saved in H5-files. The easiest way to access the results is to open H5root and open the .h5 file for plotting. Sometimes it is necessary to access the raw data, for example in order to calculate the halo parameter. This can be done either in ROOT, using the TH5Dataset library, in h5py, pytables, or by dumping the raw data to text files:

```
h5dump -d '/Step#10/x' -o s1.out -A 0 Accelerated.h5
cat s1.out | awk -F: '{print $2}' > sx10.out
```

B.4 Single particle simulations

/gpfs/home/jonnerby_j/Results/SingleParticle

B.4.1 Accelerated orbit

1. Find closed orbit initial conditions by running bash createRuns.bash. Edit the input file to get the closed orbit at the desired energy. The found initial conditions are found in Coasting.data
2. Edit the initial RF phase offset to be at an accelerated RF phase. The best way is just to scan over a range of RF values and see which are accelerating and which are decelerating.
3. Run simulations varying the initial radius and initial radial momentum around the found values by using runOPAL.
4. Run the python script

   ```
   TSGradient.py Folder
   ```

   and modify it if necessary, in order to get the r and p_r from the folder names.
5. Identify the gradient and run more simulations to find the minimum, repeat step 3.
6. When the maximum turn separation is at a minimum, cd to the simulation directory and plot the orbit of the best result by running

   ```
   python ../../plotOrbit.py
   ```

   and the turn separation with

   ```
   python ../../Turnseparation.py
   ```

B.4.2 RF Phase

/gpfs/home/jonnerby_j/Results/SingleParticle
To plot the RF phase run

```
python plotRFphase.py Folder
```

This will plot the RF phase slip of the particle with respect to the crest of the accelerating RF wave in the cavites of each RF cavity. To compare a few different phase offsets, modify the script plotRFoffset.py with the paths to the simulations.

B.4.3 Tunes

/gpfs/home/jonnerby_j/Results/SingleParticle/tunes
Edit and run the python script tunes.py to the minimum and maximum desired energy and the number of steps at which to calculate the tunes. The script will setup and run two OPAL simulations to calculate the tunes using the closed orbit finder and using the two particle mode.

B.4.4 Single particle spiral inflector injection

/gpfs/home/jonnerby_j/Results/Spiral_Inflector_single
The spiral inflector simulation is divided into two simulations, where the results of the inflector and central region are used as starting positions for the outer region. The inflector uses different fieldmaps than the outer region: the spiral inflector itself, and a 3D fieldmap of the magnetic field.

1. Find the correct scaling of the electric field and injected particle energy for the inflector by scanning:

   ```
   runOPAL.py ESCALE=START:STOP:STEPSIZE ENERGY=START:END:STEPSIZE
   ```

2. Use gnuplot to plot the vertical deflection: first start gnuplot and then run

   ```
   plot "Folder/SI-trackOrbit" u 6
   ```

   to determine which orbit is closest to $z = 0$.

When a scaling has been found that brings the particle to the midplane, the simulation should be setup in the following way:

1. Identify the correct RF phase offset by comparing RF phase outputs found in the SI.out file with the phase offsets from the well-centered orbit found earlier.
2. With the correct RF phase, run the simulation with the number of steps to bring the particle as close as possible to the handover point, e.g. at an azimuthal angle of -135 degrees. Identify the energy at the final step of the simulation.
3. Find a reasonably well-centered orbit at this energy by using the method described above. This does not have to be really optimized, since the only purpose is to again identify the correct initial RF phase offset at the handover point by comparing with the optimized solution from before.
4. When the initial RF phase offset at the handover has been found, edit the script getSingle.bash to point to the single particle inflector simulation folder. This will dump the energy, radius, radial momentum etc. into the datafile in a handover folder.
5. Run the handover simulation by using as initial position the dumped data.
6. To plot the two simulations together, copy the trackOrbit file of the inflector simulation into the folder of the handover simulation, then run bash Oneparticleinjection.bash and plotSinglePartInjection.py

B.5 Multi particle simulations

B.5.1 Matched distribution

/gpfs/home/jonnerby_j/Results/MultiParticle/193keV/RMSGradient

1. Start by generating an initial guess of the beam distribution using the matched distribution finder. This is done by running bash createRun.bash and specifying the desired energy, which at the handover point would be 193.7 keV/amu.
2. Modify the initial guess on the RMS x, y, and z by running for example a 2D scan over the initial RMS x and y, and a 1D scan over RMS z.
3. For the initial RMS x and y scans, plot the results with

   ```
   python RMSGradient.py
   ```

4. Identify the gradient: the runs with lower RMS sizes will be better matched

B.5.2 Collimation

/gpfs/home/jonnerby_j/Results/MultiParticle/193keV/Collimation/Collimator_placement
Collimation can be done either with the REMOTEPARTDEL=3 option in OPAL that removes particles further away than 3 sigma from the beam center, or by using actual collimators, which is done in the following way.

1. The collimators are placed based on a single particle orbit. Run opal aeonew.in with the initial RF phase offset etc. that you want.
2. Run

   ```
   python placeCollimators.py 8 9
   ```

   to specify at which turns the collimators should be placed. The above will place collimators between the end of turn 8 and the end of turn 9, i.e. in the 9th turn. 8 collimators are placed in each turn, at a distance of 45 degrees from each other.
3. Run bash mergetmp.bash to generate the new .tmpl file with the collimators.
4. Run the bunch simulation, at the same RF phase offset as the single particle simulation (otherwise the collimators would not be correctly placed as the orbit would be different), and specifying the gap half-width HW of the collimators.
5. To compare a few different collimator locations, repeat steps $2-4$ for each location.
6. Extract data from the simulations by running

   ```
   root plotStats.C\(\"$PWD/FOLDER/FILE.h5\"\)
   ```

   and save the generated Stat.dat files under different names.
7. Use the plot_RMS.py, plot_EMIT.py, and plot_HALO.py scripts to plot and compare the different collimator schemes.

B.5.3 Beam probes

/gpfs/home/jonnerby_j/Results/MultiParticle/193keV/Accelerated_bunch
Beam probe elements record the position of a simulation particle every time it passes through a (radial) beam probe. Beam probes are automatically placed in the templatefile using the placeCollimator.py script.

1. To extract the data from the probe .H5 files modify the loop in the bash script extractProbes.bash to loop over the beam probe files. The data will then be dumped into text files.

2. Use the python script plotHist.py to load the files and plot a logarithmic histogram of the radial distribution of the particles. The script plotOverlap.py is used to plot the radial distribution in $R - z$ space

B.5.4 Phase space plots

/gpfs/home/jonnerby_j/Results/MultiParticle/193keV/Accelerated_bunch
We can dump the position and momentum of every particle in text files for a given timestep. This can be done to for example plot the phase space during the first 12 turns.

1. To extract the data from the probe .H5 files modify the loop in the bash script extractPSx.bash to extract the data at a given turn. The data will then be dumped into text files.

2. Use the python script plotPS.py to plot the phase space with contour plots corresponding to the 1, 2, and 3 sigmas of the beam distribution.

3. The same method can be used to plot the $x - y$ space with contour plots using the python script plotXYScatter.py.

B.5.5 Movie

/gpfs/home/jonnerby_j/Results/MultiParticle/193keV/Movie
Run

```
module load root/5.34.34
root -l -n -b movie5.C\(\"$PWD/Accelerated.h5\"\)
```

to generate the frames for a movie.

Bibliography

[1] W. C. Louis, "Evidence and search for sterile neutrinos at accelerators," *Advances in High Energy Physics*, 2013. https://www.hindawi.com/journals/ahep/2013/439532/.

[2] A. Adelmann *et al.*, "Cyclotrons as drivers for precision neutrino measurements," *Advances in High Energy Physics*, 2014. http://link.aps.org/doi/10.1103/PhysRevSTAB.14.114201.

[3] A. Bungau *et al.*, "Proposal for an electron antineutrino disappearance search using high-rate ^{8}Li production and decay," *Phys. Rev. Lett.*, vol. 109, p. 141802, Oct 2012. http://link.aps.org/doi/10.1103/PhysRevLett.109.141802,.

[4] J. Yang *et al.*, "Beam dynamics simulation for the high intensity DAEδALUS cyclotrons," *Nuclear Instruments and Methods in Physics Research*, 2013. http://www.sciencedirect.com/science/article/pii/S0168900212015835.

[5] D. Winklehner, "Private communication," 2016.

[6] L. Calabretta, "Private communication," 2016.

[7] A. Rubbia, "Neutrino physics, ETH Zurich," 2015. http://neutrino.ethz.ch/Vorlesung/HS2015/Welcome.html.

[8] C. Aberle *et al.*, "Whitepaper on the DAEδALUS program," 2013. http://arxiv.org/pdf/1307.2949.pdf.

[9] M. Gordon, "Computation of closed orbits and basic focusing properties for sector-focused cyclotrons and the design of "cyclops"," *Particle Accelerators*, vol. 16, 1984. http://cds.cern.ch/record/1053175/files/p39.pdf.

[10] A. Adelmann, "Particle accelerator modeling I, ETH Zurich," 2015.

[11] P. Heikkinen, "Injection and extraction for cyclotrons, CERN Accelerator School, CERN 94-01, vol. ii," 1994. http://www.iaea.org/inis/collection/NCLCollectionStore/_Public/26/001/26001643.pdf.

[12] T. Wangler, *RF Linear Accelerators, 2nd edition*. Wiley, 2008.

[13] M. Reiser, *Theory and Design of Charged Particle Beams*. Wiley, 2008.

[14] R. Barlow *et al.*, "A precise beam dynamics model of the PSI injector 2," in *Proceedings of IPAC2013*, pp. 1020–1021. https://accelconf.web.cern.ch/accelconf/IPAC2013/papers/mopwo057.pdf.

[15] F. Chautard, "Beam dynamics for cyclotrons, CERN Accelerator School, CERN-2006-012," 2005. http://cds.cern.ch/record/813710/files/CERN-2006-012.pdf?version=1.

[16] C. Baumgarten, "Transverse-longitudinal coupling by space charge in cyclotrons," *Phys. Rev. ST Accel. Beams*, vol. 14, p. 114201, Nov 2011. http://link.aps.org/doi/10.1103/PhysRevSTAB.14.114201.

[17] M. Frey, "Semesterarbeit," 2015. http://amas.web.psi.ch/people/aadelmann/ETH-Accel-Lecture-1/projectscompleted/cse/frey-semester_thesis.pdf.

[18] H. Wiedemann, *Particle Accelerator Physics, 3rd edition*. Springer, 2007.

[19] M. Seidel, "Cyclotrons for high-intensity beams, CERN Accelerator School," 2011. https://arxiv.org/abs/1302.1001.

[20] A. Adelmann *et al.*, "The OPAL Framework: Users Reference Manual," 2016. http://amas.web.psi.ch/docs/opal/opal_user_guide.pdf.

[21] C. Allen and T. Wangler, "Parameters for quantifying beam halo," in *Proceedings of the 2001 Particle Accelerator Conference*, pp. 1732–1734. http://permalink.lanl.gov/object/tr?what=info:lanl-repo/lareport/LA-UR-01-3093.

[22] W. Barletta *et al.*, "Emittance, US Particle Accelerator School," 2010. http://uspas.fnal.gov/materials/10MIT/Emittance.pdf.